EXPERIMENTAL CONSTRAINTS ON THE MICROMECHANICS OF BRITTLE FRAGMENTATION DURING EARTHQUAKE RUPTURE

by

TROY J. BARBER

THESIS

Submitted in partial fulfillment of the
requirements for the degree of Master of Science
in Earth and Environmental Science at The
University of Texas at Arlington
December, 2016

Arlington, Texas

Supervising Committee:

W. Ashley Griffith, Supervising Professor
Qinhong Hu
Xinbao Yu

ABSTRACT

Experimental Constraints on the Micromechanics of Brittle Fragmentation during Earthquake Rupture

Troy J. Barber, MS. The University of Texas at Arlington, 2016

Supervising Professor(s): W. Ashley Griffith, Qinhong Hu, Xinbao Yu

Various fault damage fabrics, from gouge in the principal slip zone, to fragmented and pulverized rocks in the fault damage zone, have been attributed to brittle deformation at high strain rates during earthquake rupture. These fault zone fabrics are significant in terms of 1) the information they contain about coseismic deformation mechanisms, 2) the role they play in dissipating energy and contributing to slip weakening during earthquake rupture, and 3) their influence on fault rock mechanical and hydraulic properties. Past experimental work has shown that there exists a critical threshold in stress-strain rate space through which rock failure transitions from failure along a few

discrete fracture planes to pulverization. We present new experimental results on Arkansas Novaculite and Westerly Granite in which we quantify fracture surface area produced by pulverization and examine the controls of pre-existing mineral anisotropy on dissipative processes at the microscale. The results have important implications for the partitioning of dissipated energy under extreme loading conditions expected during earthquakes and the scaling of high speed laboratory rock mechanics experiments to natural fault zones.

ACKNOWLEDGEMENTS

I thank Dr. W. Ashley Griffith, my primary Supervising Professor for his inspiring leadership and unfailing belief in my potential as a burgeoning scientist. I also thank Dr. Qinhong "Max" Hu, my secondary Supervising Professor for taking a chance on a wide-eyed undergraduate and affording many opportunities to hone what were, admittedly, very raw research skills. Dr. Hamed O. Ghaffari and Christopher Borjas afforded a number of intellectual contributions to this work over many long, caffeine-fueled discussions in front of white boards. I thank Drs. Merlynd Nestell, Majie Fan, and Elizabeth Griffith specifically for the generous and unbridled use of their laboratory equipment, as well as all of the dedicated faculty and staff in the Earth and Environmental Science Department for their role in making my graduate school experience at UTA as productive and rewarding as possible. This material is based upon work supported in part by the National Science Foundation Graduate Research Fellowship Program under Grant No. (1144240) as well as the US Army 737 Research Office under grant number W911NF1410276. Any opinions, findings, and conclusions or recommendations expressed in this material are those of

the author(s) and do not necessarily reflect the views of the National Science Foundation or the US Army Research Office.

DEDICATION

To my loving wife and daughters – Lindsay, Sam, and Alex – without whom this would doubtless have been completed years ago . . by a man infinitely less satisfied with his lot in life.

TABLE OF CONTENTS

ABSTRACT ii

ACKNOWLEDGEMENTS v

TABLE OF CONTENTS vii

LIST OF FIGURES x

LIST OF TABLES xii

CHAPTER 1: GENERAL INTRODUCTION 1

1.1 Conceptual Framework 2

1.1.1 Rock fracture and fracture surface energy 2

1.1.2 Geologic faulting 8

1.1.3 The earthquake energy budget 10

1.2 Problem statement and expected outcomes 13

1.3 Experimental Methodology 14

1.3.1 The Split-Hopkinson Pressure Bar 15

1.3.2 Determination of surface area by the BET method 19

References 23

CHAPTER 2: EXPERIMENTAL CONSTRAINTS ON DYNAMIC PULVERIZATION AS A DISSIPATIVE PROCESS DURING SEISMIC SLIP 28

2.1 Introduction and Background 29

2.1.2 Introduction 29

2.1.2 Field observations of pulverized fault zone rocks 31

2.1.3 Rock pulverization in the lab 32

2.2 Methods 34

2.2.1 Specimen selection and preparation 34

2.2.2 Experimental procedure 34

2.2.3 Energy budget 36

2.2.4 Post mortem damage characterization 37

2.3 Results 39

2.3.1 Mechanical Results 39

2.3.2 Post mortem damage 43

2.4 Discussion 53

2.4.1 Fracturing as a component of dissipated energy 53

2.4.2 Implications for faulting, friction, and weakening 55

2.4.3 Open Questions 56

2.5 Conclusions 57

2.6 Acknowledgements 58

References 58

CHAPTER 3: GENERAL CONCLUSIONS 64

3.1 Summary of results 64

3.2 Contextual discussion 65

3.3 Future work 66

LIST OF FIGURES

Figure Page

1-1 Conceptual illustration of an ideal fracture composed of two fracture surfaces joined at a tipline. 2

1-2 Illustration of three basic crack displacement modes 3

1-3 Maximum principle stress (σ_1) distribution for a dynamic mode II fracture with tip at the coordinate origin as it propagates at velocity v in the positive X direction 5

1-4 a) Brittle fracture damage in rock subjected to a biaxial compressive stress state depicted by Ashby and Sammis (1990) and Bhat et al. (2012) as b) a wing-crack model consisting of a set of uniformly distributed and inclined initial flaws 7

1-5 Diagrams from Nielsen et al. (2012) detailing the evolution of the traction during seismic slip as well as the energy budget both a) at a point on a fault surface and b) over the entire fault of unit area 12

1-6 Conceptual diagram of a compressive SHPB system 17

1-7 Effect of A) pulse shaping and B) varying striker bar length and velocity on strain rate, peak stress, and loading duration during SHPB tests 19

1-8 Schematic of a generic volumetric physical adsorption analyzer 22

2-1 Conceptual diagram of a compressive SHPB system depicting the loading apparatus and associated wave travel time-distance plot..... 36

Figure Page

2-2 Qualitative classification of post mortem specimen damage for AN and WG tests. 38

2-3 Axial stress versus axial strain curves for SHPB tests on A) AN and B) WG.. 40

2-4 Peak stress versus peak strain rate experienced prior to failure shown with contours of incident pulse duration for A) AN and B) WG specimens loaded with the SHPB. 42

2-5 Histograms of particle size distribution by mass percent for dynamically pulverized specimens of A) AN and B) WG. 45

2-6 BET measured specific surface area (SSA) plotted against the inverse of radius (r^{-1}) on different size fractions of A) AN and B) WG specimens.. 47

2-7 Optical light and scanning electron microscope images of AN specimens.. 51

2-8 Scanning electron microscope images of deformed WG specimens 52

LIST OF TABLES

Table Page

2-1 Particle size and related inverse radius range used in BET specific surface area plots..... 44

2-2 Summary of fracture surface energy analysis..... 48

CHAPTER 1

GENERAL INTRODUCTION

This first chapter summarizes the framework in which this research is grounded, leading to the statement of the problem which motivates the study and the specific expected outcomes of the work, as well as a summary of the utilized methods.

Motivation

Fractures are ubiquitous in Earth's crust, yet the distribution and morphology of fracture networks in rocks is quite variable. Because of this variability, brittle damage in rocks preserves information about the processes responsible for its formation. Moreover, brittle damage strongly affects the hydraulic and elastic properties of rocks. For example, fractures and fracture networks serve as important pathways for the movement of groundwater, hydrologic contaminants, and hydrothermal fluids, as well as the flow of hydrocarbons into and out of petroleum reservoirs. In the case of low permeability rocks, fractures are the primary flow conduits. This makes characterizing brittle rock damage vital to such activities as unconventional hydrocarbon extraction and the long-term underground storage of industrial and nuclear wastes and

atmospheric CO_2. In fault zones, brittle damage can affect the evolution of fault rock strength, toughness, and permeability; exhibiting control on the mechanics of future earthquake nucleation and propagation (Lyakhovsky et al., 1997; Faulkner et al., 2006; Biegel et al., 2008). A more thorough understanding of the brittle behavior of fault zone rocks can lead to a better understanding of fundamental (and often costly and dangerous to human life) earth processes.

1.1 Conceptual Framework

1.1.1 Rock fracture and fracture surface energy

A fracture, or crack, can be defined as the existence of a displacement discontinuity (i.e. physical separation) between the particles of two opposing surfaces within a continuous solid, whose separation is very small compared to the length of the surfaces. Each surface's particles were originally adjacent and bonded to those of the opposite surface, and the surfaces are now only connected along a continuous curve called the *fracture tip* or *tipline* (Figure 1-1). Fractures tend to nucleate at material defects, which can be preexisting cracks, but also may be pores, inclusions, or any other mechanical heterogeneity (Pollard and Aydin, 1988).

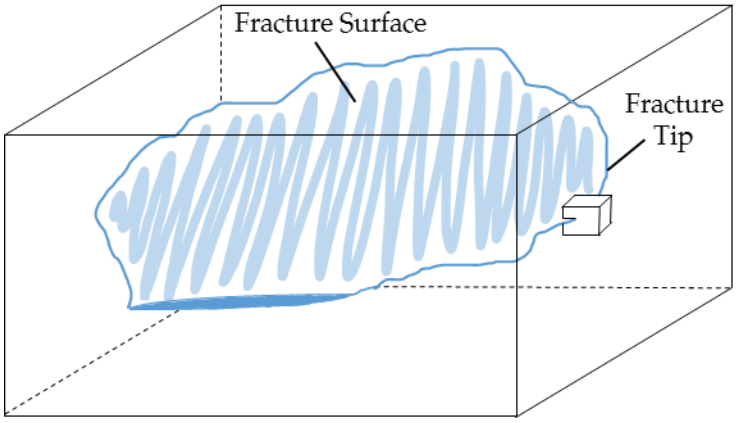

Figure 1-1. Conceptual illustration of an ideal fracture composed of two fracture surfaces joined at a tipline. Figure adapted from David Pollard's lecture notes.

The influence of an applied load in extending a fracture can be understood within the context of the parameters which characterize the stresses and strains very near the crack tip, where stresses are most apt to further break bonds and where the resulting strains will be most accommodated. Consider an ideal, flat crack of virtually zero separation. The three basic modes of relative displacement that can occur at the crack tip are illustrated in Figure 1-2, with Mode I representing the crack opening or *opening mode*, Mode II the in-plane shearing or *sliding mode*, and Mode III being the anti-plane shearing or *tearing mode*. When a crack is loaded, either directly or due to a far-field stress applied to the medium, these three basic modes can be combined in superposition to describe the general crack tip deformation fields (i.e. stress and strain fields).

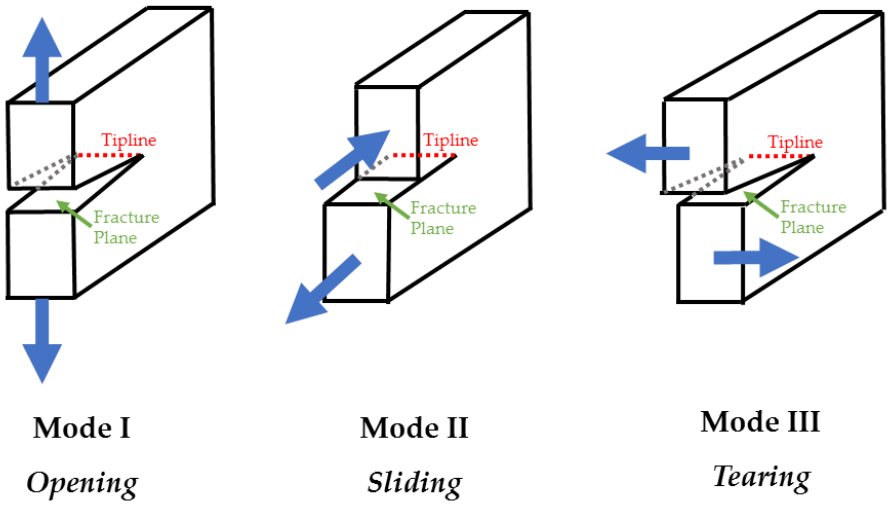

Figure 1-2. Illustration of three basic crack displacement modes. For *opening* mode or Mode I, the displacement discontinuities of particles on the fracture surfaces are perpendicular to the fracture plane and perpendicular to the tipline; For *sliding* mode or Mode II, the displacement discontinuities are parallel to the fracture plane and perpendicular to the tipline; For *tearing* or Mode III, the displacement discontinuities are parallel to the fracture plane and parallel to the tipline.

In linear elastic fracture mechanics (LEFM), the stress, displacement, and velocity fields developed around fracture tips can be derived by solving the Airy stress function subject to appropriate boundary conditions (e.g., Mushkhelishvili, 1953; Pollard and Segall, 1987). For stationary or *quasi-static* cracks, stress fields exhibit the following important characteristics:

I. The amplitude of the field is proportional to the instantaneous *stress intensity factor*, K_m (where index m refers to fracture mode I, II, or III).

II. The field has an inverse square root dependence on the distance from the crack tip, r.

III. The field varies as a function, $\sum_{ij}^{m}(\theta)$, of angular position around the fracture tip (where indices *i* and *j* take the values of 1-3).

Freund (1998) applied these relationships to the asymptotic solution of an in-plane, *dynamic* (fast moving) fracture propagating through an isotropic elastic solid at sub-Rayleigh velocity. In his solutions, the functions which represent the angular variation of stress components depend also on the instantaneous *crack tip speed,* v. For a dynamic mode II rupture propagating at velocity, *v*, as illustrated in Figure 1-3, the asymptotic near-tip stress distribution can be approximated by:

$$\sigma_{ij} = \frac{K_{II}}{\sqrt{2\pi r}} \sum_{ij}^{II}(\theta, v) \qquad (1)$$

An outstanding takeaway is that remote stress is hugely intensified very near a crack tip, and that the near-tip stress intensification is rate dependent with respect to the propagation velocity of the crack.

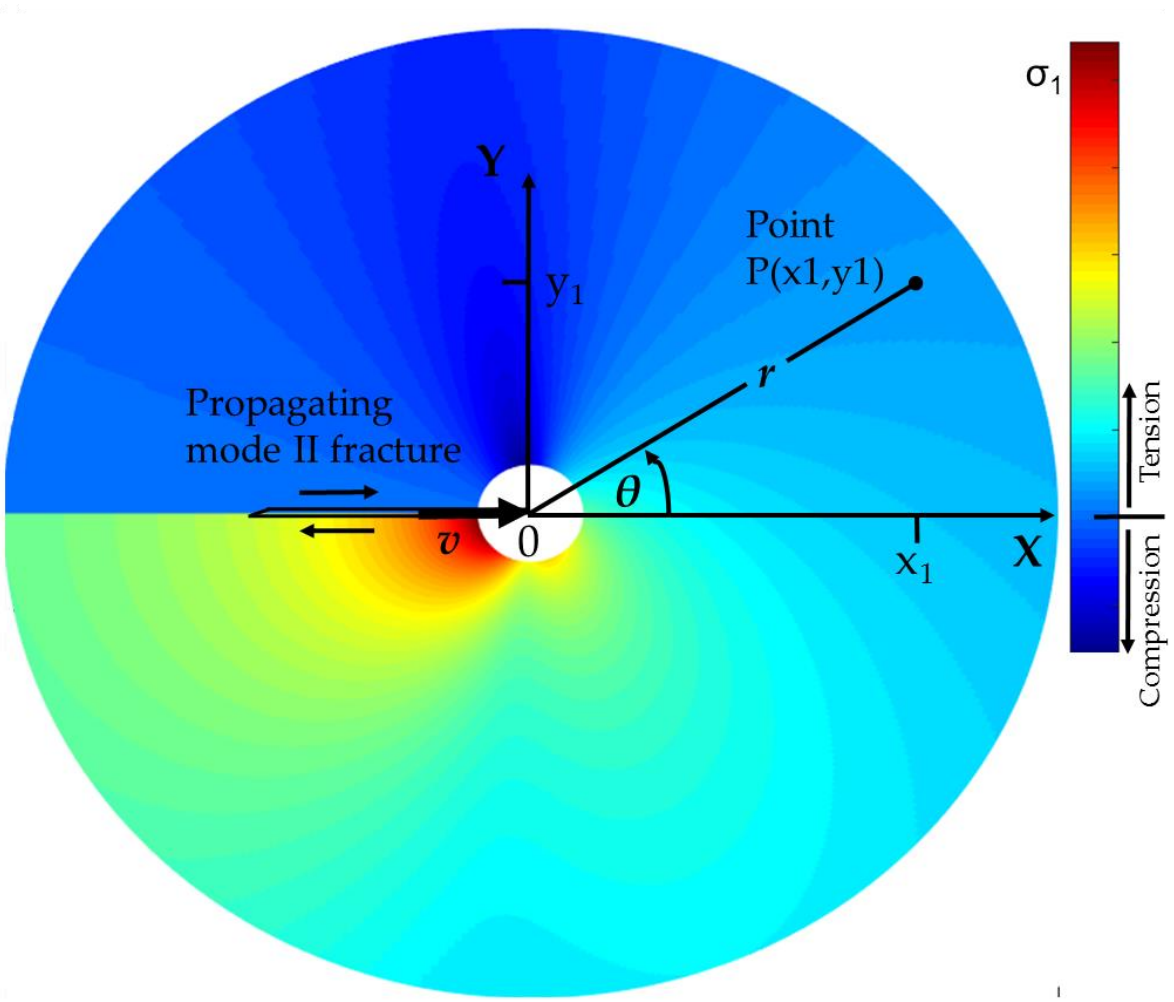

Figure 1-3. Maximum principle stress (σ_1) distribution for a dynamic mode II fracture with tip at the coordinate origin as it propagates at velocity v in the positive X direction. Deformation states at any point P(x_1,y_1) are calculated for the relative position (r, θ) of the propagating fracture. Figure based on solutions in the form presented by Reches and Dewers (2005).

During propagation of an LEFM crack, the change in mechanical energy associated with an increment of crack growth is equal in magnitude to the amount of *surface energy*, γ, per unit crack area required to produce the additional crack surface (Griffith, 1921). This change in energy, commonly abbreviated as simply *G*, is referred to as the

strain energy release rate or *fracture energy*. Irwin (1958) showed that, for plane stress, the fracture energy of a mode I fracture is directly proportional to the square of the mode I stress intensity factor, K. This leads to a crack growth criterion in terms of a critical stress intensity factor, K_{Ic}, or a critical value of the energy release rate, G_c (Jaegar et al, 2009), with the relation

$$G_c = \frac{{K_{Ic}}^2}{E} = 2\gamma \qquad (2)$$

where E is the Young's Modulus of the material. This criterion when considered in conjunction with Freund's asymptotic solution for a dynamic fracture permits the relation of deformation fields associated with a propagating crack to the total new crack surface area created, and thereby, the amount of energy consumed during crack extension.

These fundamental concepts in fracture mechanics have been integrated into continuum models of rock strength. Ashby and Sammis (1990) formulated a popular model framework for understanding rock failure under quasi-static loading conditions premised on the growth and interaction of existing microscale cracks. The model considers a rock containing a uniform distribution of initial flaws (cracks) oriented at a fixed angle and subjected to a biaxial (σ_1,σ_3) compressive stress state (Figure 1-4). At the tips of these inclined starter flaws, wing cracks nucleate and propagate in the direction of σ_1. As the growth of these wing cracks is governed by the stress intensity at the crack

tips, the failure strength of the rock, in bulk, is controlled by the fracture toughness of the rock material. Bhat et al. (2012) later extended this model to consider the effect of dynamic crack growth associated with loading at high strain rates.

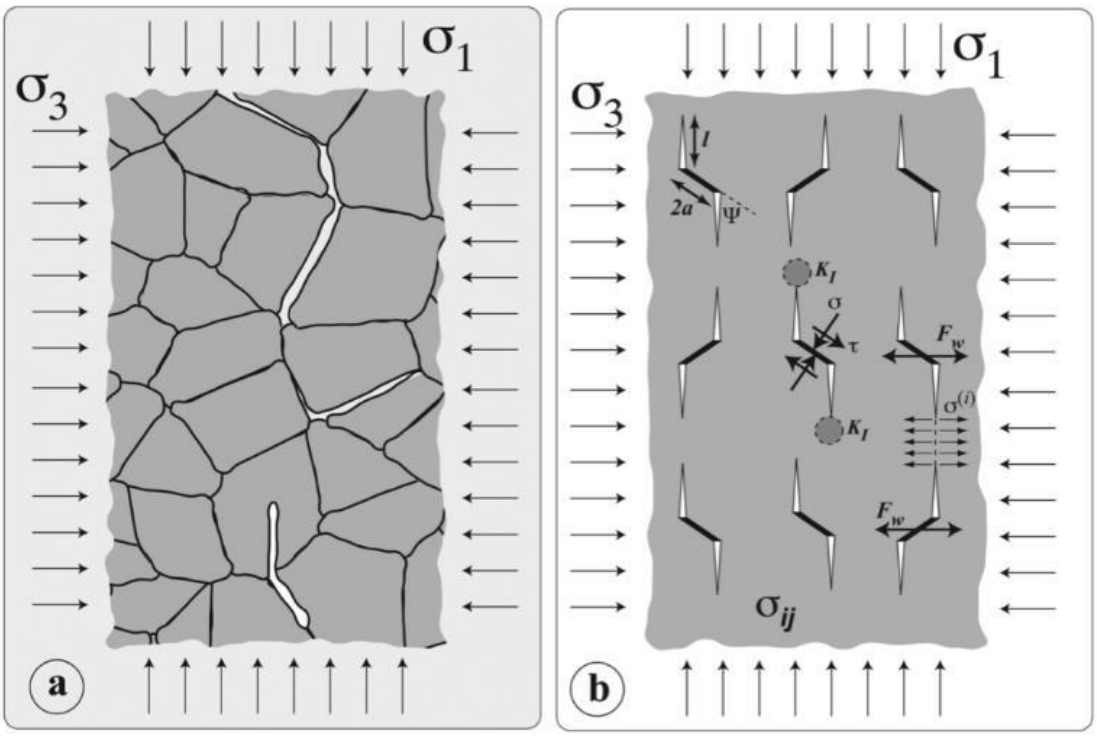

Figure 1-4 – a) Brittle fracture damage in rock subjected to a biaxial compressive stress state depicted by Ashby and Sammis (1990) and Bhat et al. (2012) as b) a *wing-crack* model consisting of a set of uniformly distributed and inclined initial flaws. Shear strain along the flaws promotes propagation through coalescing tensile wing cracks.

The macroscopic failure mode in rocks exhibits a strain rate dependence, passing through a critical high strain rate transition (Doan and Gary, 2009; Yuan et al., 2011). At lower strain rates, brittle failure is achieved via localized, through-going fractures,

whereas high strain rates lead to pervasive, intersecting fractures and, eventually, bulk failure through intense fragmentation. In nature, this transition is demonstrated by intensely pulverized rocks that are associated with fast loading-rate events like earthquake rupture, explosive volcanic eruption, and bolide impact, as well as events related to human activity (e.g. mining, excavation, military operations). When exposed to these extreme loading conditions, rocks spanning a wide range in composition and grain size are often reduced to 10s of micrometer sized fragments (Reches and Dewers, 2005; Key and Schultz, 2011; Rockwell et al., 2009; Rempe et al., 2013). Historically, mechanical grain size reduction of this magnitude in rocks has been associated with comminution in fault cores that have experienced high amounts of shear strain. Yet many pulverized rocks occur 10s to 100s of meters from the fault core and preserve original grain boundaries, with minimal evidence of grain rotation or shear subsequent to fragmentation (Reches and Dewers, 2005; Yuan et al., 2011). Whereas the mechanism attributed to pulverizing rocks in fault damage zones is an active area of research, consensus indicates an association with dynamic rupture propagation approaching, or in some cases exceeding, the shear wave speed (Doan and Gary, 2009; Yuan et al., 2011; Mitchell et al., 2011; Rempe et al., 2013; Fondriest et al., 2015; Aben et al., 2016).

1.1.2 Geologic faulting

Geologic faults are a subcategory of fracture, wherein the discontinuity occurs between two rock masses along which relative lateral (i.e. parallel to the fault surface) displacements have occurred. The relative displacement along a fault is referred to as *slip*. While often contemporaneous, slip is not to be confused with *rupture*, which describes the breaking of cohesion along a fault surface and extension of the fault tipline or *front*. A common lay misconception about large-scale geologic faults is that they exist as continuous, open discontinuities extending deep into the earth's crust. Most large-scale faulting can best be described in terms of geometrically and mechanically complex fault zones composed of discrete fault segments, which may or may not coalesce. Beyond even very shallow depths, these fault surfaces aren't often discontinuities at all, but exist as healed planes of inherent weakness during the inter-seismic period. Therefore, for slip along a fault surface to occur, a rupture front must first nucleate from some discrete area and radiate out from that nucleation point until the rate of energy release no longer exceeds the energy required to create or reactivate new fault surface area.

Faults exist within the earth's crust across approximately 12 orders of magnitude (μm to thousands of km) in length scale. However, faults that can generate seismicity (i.e. earthquakes) tend to exist at a length scale much greater than many rock

heterogeneities. Therefore, geologic formations can, as a first-order approximation, be conveniently modeled as continuum materials and, likewise, seismic faults can be modeled as idealized LEFM cracks. The utility in doing so is plain, as the stress and strain fields within the crust can thus be implemented into continuum-based models of fault nucleation and propagation. It is important to note that geologic faults do not conform to the description of LEFM cracks, and the convenience of modeling them as such comes at the cost of working under some unrealistic assumptions. Ultimately, those assumptions must be loosened and models must be revised to glean insight from applying LEFM models to real fault zones. They are, nonetheless, an instructive springboard into more detailed analyses of the mechanics of faulting.

1.1.3 The earthquake energy budget

When seismic slip occurs, frictional resistance on the fault surface drops with slip acceleration in a process known as *slip weakening*. Concomitantly, gravitational and elastic strain energy that is stored in the crust is rapidly released in the form of seismic waves (kinetic energy), frictional heat (thermal energy), and various other energy sinks such as the energy dissipated in phase transitions (e.g. solid to melt), plastic deformation, or the creation of new fracture surfaces. Analysis of seismic waves can yield estimates of the seismic energy radiated during an earthquake, but seismology

alone is incapable of partitioning the energy dissipated via heat and other sinks during the weakening phase of slip, collectively referred to in the seismological literature as *breakdown work* or *fracture energy*. It is worth noting that, despite its unfortunate naming, seismological fracture energy does not simply represent the energy dissipated in creating new fracture surface area as with the LEFM crack, but rather serves as a macroscopic analogue representing the collective components of energy dissipated on a fault of unit area during the slip weakening phase of the seismic cycle (Figure 1-5.b), which includes but is not limited to Griffith's *fracture surface energy*.

Because the mechanics of earthquake rupture are controlled, in part, by the balance between the various energy sinks at play, an outstanding aim in current earthquake research involves constraining the components of the earthquake energy budget and their role in governing processes like slip weakening. Traditional avenues for investigating earthquake mechanics cannot directly observe the physicochemical processes active on the fault surface during the seismic cycle. The violent and transient occurrence of an earthquake rupture is both unpredictable and largely inaccessible. Beyond drilling into active faults – a costly endeavor which samples a limited volume and to a relatively shallow maximum depth – researchers are consigned to employ an interdisciplinary suite of limited approaches in studying the earthquake energy budget.

A number of investigations of exhumed fault zones have attempted to quantify the surface area of fault gouge in the principal slip zone (PSZ) as well as off-fault cracking and brittle damage accumulation within the greater fault damage zone to estimate the surface energy component of breakdown work (Olgaard and Brace, 1983; Chester et al., 2005; Wilson et al., 2005; Keulen et al., 2007; Rockwell et al., 2009; Wechsler et al., 2011; Aben et al. 2016). Several challenges exist for this practice. For mature faults, estimating the number of seismic events which have contributed to the damage measured can be difficult. Moreover, damage distribution along faults is heterogeneous, and the choice of representative elementary volume of rock to subsample can drastically change resulting surface area estimates. The identification of pseudotachylyte veins on some exhumed faults allows for the estimation of thermal energy and latent heat dissipated during dynamic frictional slip (Kanamori et al., 1998; Di Toro et al., 2005; Pittarello et al., 2008).

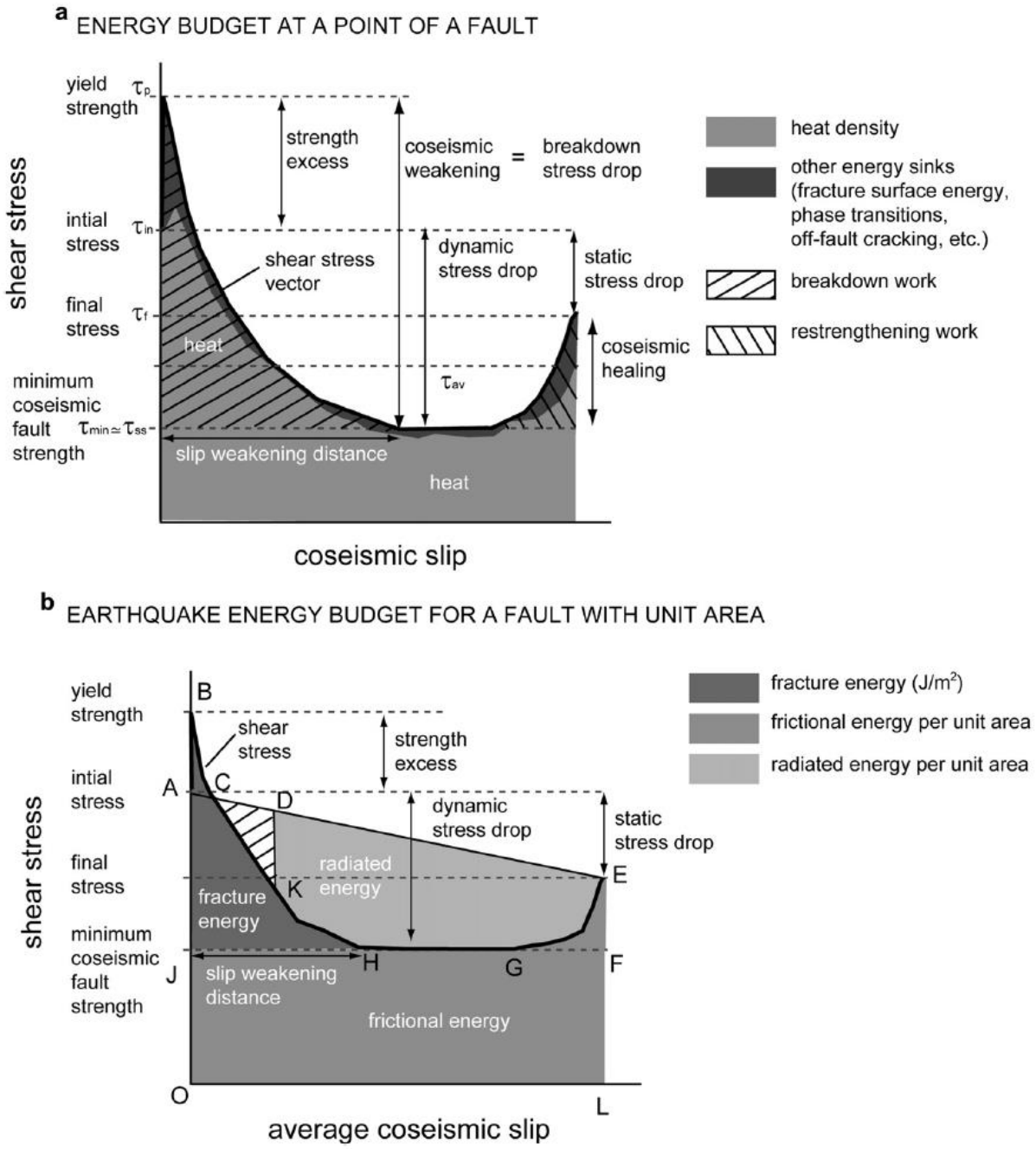

Figure 1-5. Diagrams from Niemeijer et al. (2012) detailing the evolution of the traction during seismic slip as well as the energy budget both a) at a point on a fault surface and b) over the entire fault of unit area. Similar diagrams are obtained in dynamic rock friction experiments and used by both seismologists and rock mechanics experimenters to glean information about energy partitioning during natural and laboratory dynamic rupture. The breakdown work in (a) is the area defined by the shear stress curve and the minimum coseismic fault strength (which includes all the fracture surface energy).

This approach hinges on an assumption that the amount of frictional work dissipated as thermal energy during coseismic slip is proportional to the volume of melt generated, but, as with brittle damage accumulation, the possibility of melt contribution from multiple seismic events exists and the scarcity of such features suggests that they may not serve as indicators of any ubiquitous fault mechanical process. Nonetheless, pseudotachylytes serve as an interesting feature, as the presence of melt during coseismic slip offers a possible solution to the debate over true fault strength and the mechanisms by which slip weakening might occur. These field-based estimates are usually contextualized in terms of theoretical predictions from dynamic rupture models (Reches and Lockner, 1994; Rice et al., 2005; Andrews, 2005) as well as laboratory analogs such as dynamic loading experiments (Doan and Gary, 2009; Yuan et al., 2011; Doan and D'Hour, 2012; Aben et al., 2016) and high-speed friction tests on fault rock materials (Han et al., 2007; Di Toro et al., 2011; Togo and Shimamoto, 2011; Lyakhovsky et al., 2014). However, issues of scaling arise when comparing loading conditions and damage fabrics induced on cm-scale laboratory specimens with conditions observed on m- to km-scale fault zone rocks.

1.2 Problem statement and expected outcomes

Fault damage zones represent the sum total of many processes acting on faults during both the coseismic and interseismic phases of the seismic cycle (Savage and Brodsky, 2009). Recent attempts to constrain the energy dissipated in the creation of new fracture surfaces within fault damage zones have led to some disagreement as to whether fracture surface energy constitutes a significant portion of the overall energy budget of earthquakes, with estimates ranging from 1% (Chester et al., 2005; Rockwell et al., 2009) to as much as 50% (Reches and Dewers, 2005; Wilson et al., 2005). Moreover, the identification of inexplicably wide swaths of pulverized rocks adjacent to faults have raised questions as to the physical mechanisms for pulverization, particularly as they affect earthquake propagation and frictional slip. Here we attempt to expand our knowledge of the rock fragmentation and pulverization mechanism by 1) exploring the effect of the complete load path on the transition from discrete fracture to pulverization and 2) quantifying the degree of comminution (fragment size reduction) that occurs across this transition with consideration to the energy sink represented by the pulverization process.

1.3 Experimental methodology

The objectives of this research were approached through a series of dynamic loading experiments on select rock specimens using a Split-Hopkinson Pressure Bar (SHPB)

followed by post-mortem damage characterization via scanning electron microscopy (SEM) and specific surface area measurement using the Brunauer–Emmett–Teller (BET) gas adsorption method. In this section, we outline the theory and operation of the SHPB, followed by a brief description of how gas adsorption is used to measure the accessible surface area of a solid.

1.3.1 The Split-Hopkinson Pressure Bar

Study of the inelastic response of rock to loading at strain rates less than 10^{-2} s^{-1} is a mature and well-documented field of research; however, testing of geologic materials has only just scratched the surface in the area of brittle deformation at higher strain rates (10^{0} ~ 10^{6} s^{-1}). Of the available techniques capable of dynamic loading at high strain rates, the SHPB holds a singular advantage in that the loading apparatus has dual functionality: both loading and monitoring specimen deformation via strategically-placed strain gauges along the incident and transmitted bars, allowing complete capture of the transient stress and strain history of the specimen. Consistent with other dynamic compression tests on brittle materials, SHPB tests on rock exhibit the following standout characteristics: 1) The dynamic uniaxial compressive strength (UCS) increases from its quasi-static value with increasing loading rate; 2) This increase in strength is

accompanied by an increase in the brittle damage; and 3) a marked increase in the energy dissipated in damaging the specimen. The correspondence between fast loading rate, strength/energy consumption increase, and increase in fracture surface area has been recognized and documented qualitatively using optical and scanning electron microscopy (Lundberg 1976; Ravi-Chandar & Yang 1997; Zhang et al. 1999; Xia et al. 2008). However, in the geologic literature very few efforts to directly measure the energy partitioned into fracture growth during dynamic loading of rocks have been documented.

The SHPB system consists of a loading apparatus and a system for monitoring mechanical response (Figure 1-6.A). The instrument operates by firing the striker bar, the velocity of which is monitored with optical sensors located on the gun barrel. The striker impacts the incident bar, generating a compressive wave (incident pulse) which travels along the incident bar toward the cylindrical specimen sandwiched between the incident and transmitted bars. Striker bar length controls the load duration experienced by the specimen, and varying the striker bar impact speed changes the loading rate and stress amplitude. Upon reaching the specimen, part of the wave energy (reflected pulse) is reflected from the incident bar/specimen interface back along the incident bar. The remaining wave energy (transmitted pulse) is transmitted through the specimen/transmission bar interface and absorbed by a bar stop at the end of the

transmission bar. The strain gauges record the incident, reflected, and transmitted waves (Figure 1-6.B), which Kolsky (1949) showed can be related to the instantaneous stress, $\sigma_s(t)$, strain, $\varepsilon_s(t)$, and strain rate, $\dot{\varepsilon}_s(t)$, in the specimen as

$$\sigma_s(t) = \frac{A_b}{A_s} E_b \varepsilon_T(t) \quad (3)$$

$$\varepsilon_s(t) = \int_0^t \dot{\varepsilon}_s(t)dt \quad (4)$$

$$\dot{\varepsilon}_s(t) = -2\frac{C_b}{L_s} \varepsilon_R(t) \quad (5)$$

where ε_R and ε_T represent the bar strain associated with the reflected and transmitted pulses, respectively; A_b, E_b, C_b represent the cross-sectional area, Young's modulus, and longitudinal wave speed of the steel bars, respectively; and A_s and L_s are the cross sectional area and length of the specimen, respectively. The above equations are derived considering 1D wave propagation (no dispersion) along the bars and stress equilibrium (i.e. $\varepsilon_I(t) + \varepsilon_R(t) = \varepsilon_T(t)$; Figure 1-6.C) between the specimen faces throughout the loading duration. In the SHPB configuration used in this study, a momentum trap mounted on the incident bar prevents the sample from being loaded by multiple reflections of the incident wave, thereby limiting the sample to a single loading pulse.

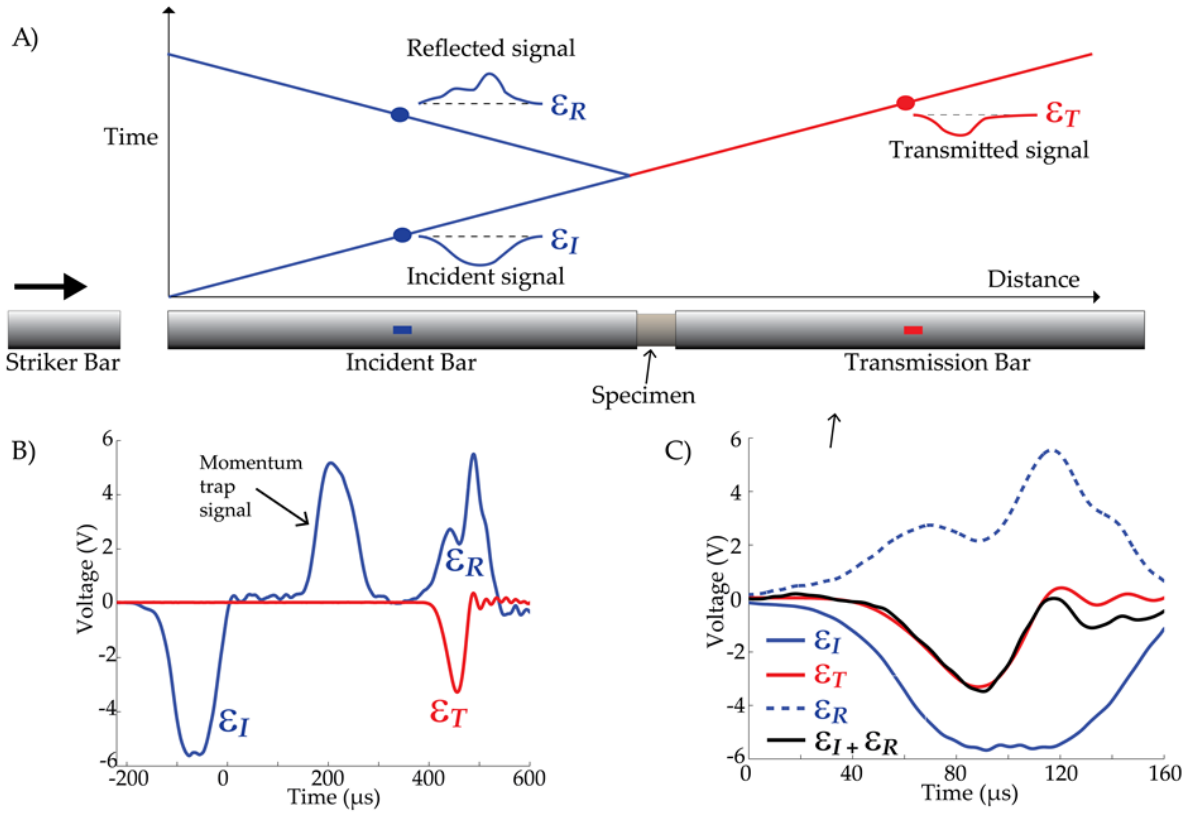

Figure 1-6. Conceptual diagram of a compressive SHPB system depicting A) the loading apparatus and associated wave travel time-distance plot. B) Example of raw voltage signal collected during a test. The blue and red curves represent voltage in the incident and transmitted bar strain gages, respectively. Note the waveform in the incident bar signal occurring at ~200 μs, which is generated by the momentum trap, and does not interact with the specimen. C) Illustration of dynamic force balance at the specimen-bar interfaces. According to 1D wave theory, the force on the incident bar-specimen interface is proportional to the sum of the incident and reflected pulses, $\varepsilon_I(t)+\varepsilon\varepsilon_R(t)$, and the force on the transmitted bar-specimen interface is proportional to the transmitted pulse, $\varepsilon_T(t)$.

In a traditional SHPB test, impact of the striker bar directly onto an incident bar generates a rectangular waveform with a sharp rise time and characteristic high frequency oscillations (Chen & Song 2013). Earlier efforts to characterize the response of brittle materials by dynamic loading revealed that this rectangular waveform is poorly suited to establish stress equilibrium and constant strain rate within the

specimen (Li et al. 2000; Chen & Song 2013). Davies & Hunter (1963) showed that the critical time necessary for the state of stress to equilibrate within the specimen is $t_c = \pi L_s/C_s$, where L_s is the specimen length and C_s is the elastic wave speed within the specimen. Thus, the constitutive dynamic failure strain (ε_c) in the specimen material dictates a size dependent limit on the achievable constant strain rate in a SHPB experiment as $\dot{\varepsilon}_c = \varepsilon_c/t_c = \varepsilon_c C_s/\pi L_s$. Moreover, too sharp a rise time precludes the establishment of stress equilibrium prior to brittle failure of the material, and any dispersive oscillations in the rectangular waveform can translate to equally high-frequency oscillations in the dynamic constitutive response curves of the material being tested. A common practice to avoid these undesirable qualities in the incident loading pulse is to place a thin disc of ductile material on the impact end of the incident bar. Figure 1-7 illustrates how this disc acts to shape the incident pulse to one which facilitates stress equilibrium and constant strain rate within the specimen up to failure.

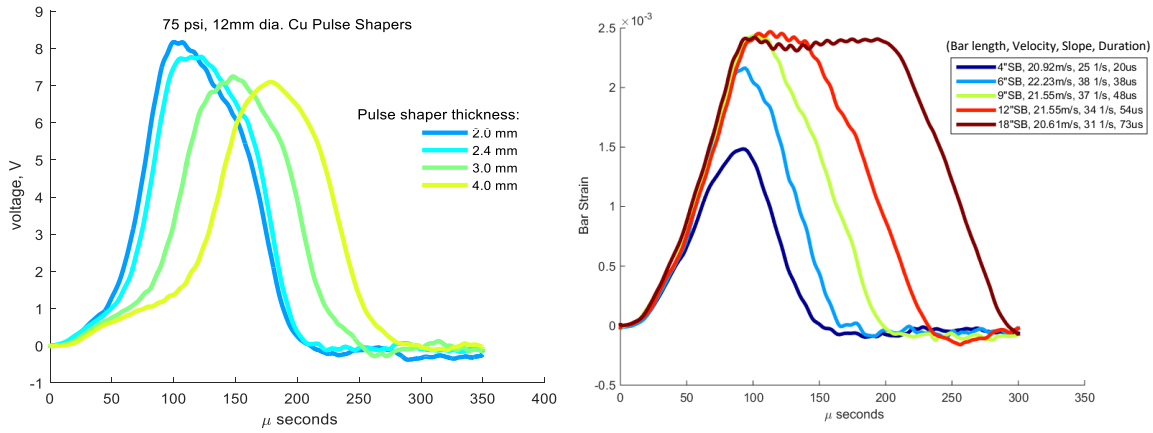

Figure 1-7. Effect of A) pulse shaping and B) varying striker bar length and velocity on strain rate, peak stress, and loading duration during SHPB tests. Varying the thickness of copper pulse shaper changes the rise time of the voltage in the strain gauge, which is proportional to the strain rate experienced by the specimen. At a fixed impact velocity, varying the bar length changes the duration and, thus, amplitude of the stress pulse, while maintaining a fixed strain rate.

1.3.2 Determination of surface area by the BET method

For laboratory specimens damaged very near or beyond the critical strain rate transition to pulverization, post mortem specimen material is highly fragmented or pulverized to a fine powder. As such, thin sectioning and observation with optical or scanning electron microscopy is not ideal for such specimens. As an explicit goal of this work is to quantify the fracture energy consumed in the creation of specimen fragments under dynamic compressive loading conditions, the total accessible fragment surface area of select post-mortem specimens is measured using gas adsorption and analyzed according to the Brunauer, Emmet, and Teller (BET) method (Brunauer et al., 1938). The geometric surface area of an undamaged specimen is negligible (<< 1%) compared to the

total surface area of a pulverized specimen. Therefore, the BET measured surface area is taken to represent the total new fracture surface area created during a single loading event. Fracture surface area measurements are used to calculate equated estimates of the portion of energy dissipated in the creation of new surface area during a single pulverization event.

A common practice is to estimate collective particle surface area using size distributions (e.g. Yoshioka 1986; Wilson et al. 2005; Rockwell et al. 2009). Popular tools used for measuring particle size such as Coulter counters and mechanical sieves tend to size particles according to their smallest dimension, but give no information on particle shape, leading to an underestimation of surface area (e.g., Olgaard and Brace, 1983). This necessitates the assumption of some representative surface roughness to bring about more accurate estimates of real particle surface area. Gas adsorption offers an advantage over estimates of new crack surface area based on simple particle size analysis in that gases can account directly for surface roughness and penetrate cracks intersecting particle surfaces.

The BET method considers the quantity of adsorbate gas molecules of effective surface area, A_m, adsorbed onto the accessible surfaces of an adsorbent material. Adsorption is assumed to be a monolayer at very low pressure and modelled as a function of gas pressure and temperature. The basic components of a volumetric

physical adsorption analyzer include: a liquid nitrogen cold bath, sample cell, vacuum pump, adsorptive gas source, temperature and pressure sensors, and a signal recorder. The technique is carried out by evacuating the sample chamber while immersed in a liquid nitrogen cold bath to maintain a constant low temperature, and then very slowly introducing adsorptive gas in measured increments. As the gas molecules adsorb onto the specimen surface, the pressure inside the specimen chamber equilibrates and both the quantity of gas introduced and pressure are recorded. The BET equation (Gregg and Sing, 1982) models the monolayer adsorption gas volume per unit sample mass, V_m [cm3 (STP)/g], as

$$\frac{p}{V_a(p_0-p)} = \frac{1}{V_m C} + \frac{C-1}{V_m C}(p/p_0) \qquad (6)$$

Where V_a is the total volume of adsorbate gas introduced, p and p_0 are the isothermal equilibrium and saturation pressures of the adsorbate, respectively, and C is the adsorption constant. Plotting $\frac{p}{V_a(p_0-p)}$ against (p/p_0) yields a linear relationship from which V_m can be extracted (Figure 1-8,B).

The total surface area of sample contained within the sample cell, SA, is related to the monolayer adsorption volume, V_m, as

$$SA = \frac{V_m N A_m}{M_V} \qquad (7)$$

Where N is Avogadro's number, A_m is the adsorption cross section of the adsorbate species, and M_V is the molar volume of the adsorbate species.

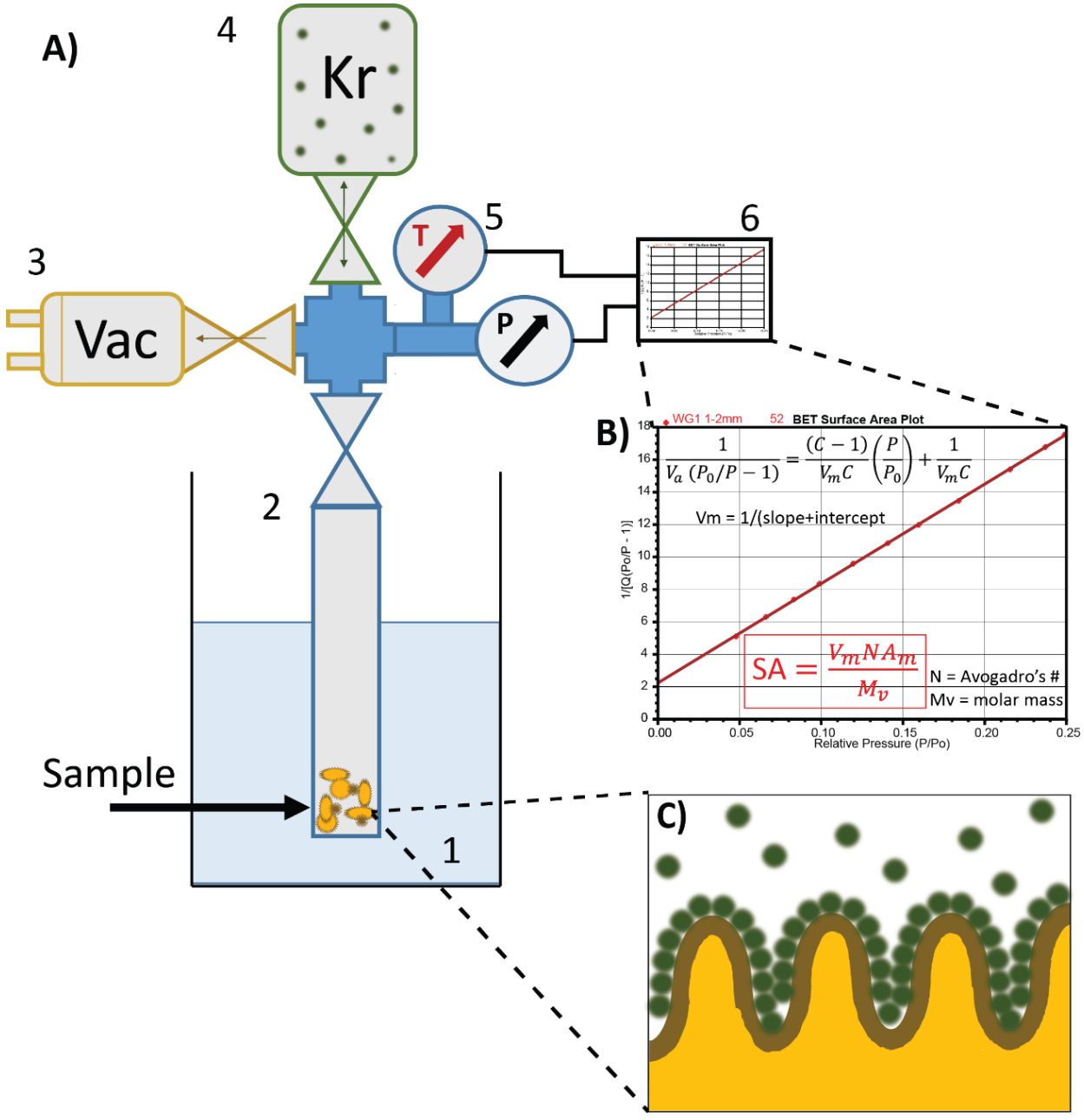

Figure 1-8. A) Schematic of a generic volumetric physical adsorption analyzer comprised of (1) liquid nitrogen cold bath, (2) sample cell, (3) vacuum pump, (4) adsorptive gas source (here Kr), (5)

temperature sensor and pressure transducer, and (6) signal recorder. B) Typical BET specific surface area plot. Relating monlayer volume of gas adsorbed, V_m, to isothermal relative pressure, P/P_0, yields the surface area, SA, of specimen. C) Idealization of gas molecules of effective surface area, A_m, adsorbing to the surface of a rough specimen.

References

1. Lyakhovsky, V., Ben-Zion, Y. and Agnon, A., 1997. Distributed damage, faulting, and friction. *Journal of Geophysical Research: Solid Earth*, *102*(B12), pp.27635-27649.
2. Faulkner, D.R., Mitchell, T.M., Healy, D. and Heap, M.J., 2006. Slip on'weak'faults by the rotation of regional stress in the fracture damage zone. *Nature*, *444*(7121), pp.922-925.
3. Biegel, R.L., Sammis, C.G. and Rosakis, A.J., 2008. An experimental study of the effect of off-fault damage on the velocity of a slip pulse. *Journal of Geophysical Research: Solid Earth*, *113*(B4).
4. Pollard, D.D. and Aydin, A., 1988. Progress in understanding jointing over the past century. *GSA Bulletin*, *100*(8), pp.1181-1204.
5. Muskhelishvili, N. I. (1953). Some basic problems of the mathematical theory of elasticity, 3rd edition, Groningen: Noordhoff.
6. Pollard, D. D., & Segall, P. (1987). Theoretical displacements and stresses near fractures in rock: with applications to faults, joints, veins, dikes, and solution surfaces. *Fracture mechanics of rock*, *277*(349), 277-349.
7. Freund, L. Benjamin, 1998. ed. "Dynamic fracture mechanics." Cambridge university press.
8. Reches, Z. & Dewers, T. a. 2005 Gouge formation by dynamic pulverization during earthquake rupture. *Earth Planet. Sci. Lett.* **235**, 361–374. (doi:10.1016/j.epsl.2005.04.009)
9. Griffith, A.A., 1921. The phenomena of rupture and flow in solids. *Philosophical transactions of the royal society of london. Series A, containing papers of a mathematical or physical character*, 221, pp.163-198.

10. Irwin, G. R., J. A. Kies, and H. L. Smith. "Fracture strengths relative to onset and arrest of crack propagation." *Proc. ASTM*. Vol. 58. 1958.

11. Jaeger, John Conrad, Neville GW Cook, and Robert Zimmerman. "Fundamentals of rock mechanics." John Wiley & Sons, 2009.

12. Ashby, M.F. and Sammis, C.G., 1990. The damage mechanics of brittle solids in compression. *Pure and Applied Geophysics*, *133*(3), pp.489-521.

13. Bhat, H.S., Rosakis, A.J. and Sammis, C.G., 2012. A micromechanics based constitutive model for brittle failure at high strain rates. *Journal of Applied Mechanics*, *79*(3), p.031016.

14. Doan, M.L. and Gary, G., 2009. Rock pulverization at high strain rate near the San Andreas fault. *Nature Geoscience*, *2*(10), pp.709-712.

15. Yuan, F., Prakash, V. and Tullis, T., 2011. Origin of pulverized rocks during earthquake fault rupture. *Journal of Geophysical Research: Solid Earth*, *116*(B6).

16. Key, W.R. and Schultz, R.A., 2011. Fault formation in porous sedimentary rocks at high strain rates: First results from the Upheaval Dome impact structure, Utah, USA. *Geological Society of America Bulletin*, *123*(5-6), pp.1161-1170.

17. Rockwell, T., Sisk, M., Girty, G., Dor, O., Wechsler, N. and Ben-Zion, Y., 2009. Chemical and physical characteristics of pulverized Tejon Lookout Granite adjacent to the San Andreas and Garlock faults: implications for earthquake physics. In *Mechanics, Structure and Evolution of Fault Zones* (pp. 1725-1746). Birkhäuser Basel.

18. Rempe, M., Mitchell, T., Renner, J., Nippress, S., Ben-Zion, Y. and Rockwell, T., 2013. Damage and seismic velocity structure of pulverized rocks near the San Andreas Fault. *Journal of Geophysical Research: Solid Earth*, *118*(6), pp.2813-2831.

19. Mitchell, T.M., Ben-Zion, Y. and Shimamoto, T., 2011. Pulverized fault rocks and damage asymmetry along the Arima-Takatsuki Tectonic Line, Japan. *Earth and Planetary Science Letters*, *308*(3), pp.284-297.

20. Fondriest, M., Aretusini, S., Di Toro, G. and Smith, S.A., 2015. Fracturing and rock pulverization along an exhumed seismogenic fault zone in dolostones: The Foiana Fault Zone (Southern Alps, Italy). *Tectonophysics*, *654*, pp.56-74.

21. Aben, F.M., Doan, M.L., Mitchell, T.M., Toussaint, R., Reuschlé, T., Fondriest, M., Gratier, J.P. and Renard, F., 2016. Dynamic fracturing by successive coseismic loadings leads to pulverization in active fault zones. *Journal of Geophysical Research: Solid Earth*, *121*(4), pp.2338-2360.

22. Niemeijer, A., Di Toro, G., Griffith, W.A., Bistacchi, A., Smith, S.A. and Nielsen, S., 2012. Inferring earthquake physics and chemistry using an integrated field and laboratory approach. *Journal of Structural Geology*, *39*, pp.2-36.

23. Olgaard, D.L. and Brace, W.F., 1983, February. The microstructure of gouge from a mining-induced seismic shear zone. In *International Journal of Rock Mechanics and Mining Sciences & Geomechanics Abstracts* (Vol. 20, No. 1, pp. 11-19). Pergamon.

24. Chester, J.S., Chester, F.M. and Kronenberg, A.K., 2005. Fracture surface energy of the Punchbowl fault, San Andreas system. *Nature*, *437*(7055), pp.133-136.

25. Wilson, B., Dewers, T., Reches, Z.E. and Brune, J., 2005. Particle size and energetics of gouge from earthquake rupture zones. *Nature*, *434*(7034), pp.749-752.

26. Keulen, N., Heilbronner, R., Stünitz, H., Boullier, A.M. and Ito, H., 2007. Grain size distributions of fault rocks: A comparison between experimentally and naturally deformed granitoids. *Journal of Structural Geology*, *29*(8), pp.1282-1300.

27. Wechsler, N., Allen, E.E., Rockwell, T.K., Girty, G., Chester, J.S. and Ben-Zion, Y., 2011. Characterization of pulverized granitoids in a shallow core along the San Andreas Fault, Littlerock, CA. *Geophysical Journal International*, *186*(2), pp.401-417.

28. Kanamori, H., Anderson, D.L. and Heaton, T.H., 1998. Frictional melting during the rupture of the 1994 Bolivian earthquake. *Science*, *279*(5352), pp.839-842.

29. Di Toro, G., Pennacchioni, G. and Teza, G., 2005. Can pseudotachylytes be used to infer earthquake source parameters? An example of limitations in the study of exhumed faults. *Tectonophysics*, *402*(1), pp.3-20.

30. Pittarello, L., Di Toro, G., Bizzarri, A., Pennacchioni, G., Hadizadeh, J. and Cocco, M., 2008. Energy partitioning during seismic slip in pseudotachylyte-bearing faults (Gole Larghe Fault, Adamello, Italy). *Earth and Planetary Science Letters*, *269*(1), pp.131-139.

31. Reches, Z.E. and Lockner, D.A., 1994. Nucleation and growth of faults in brittle rocks. *Journal of Geophysical Research: Solid Earth*, *99*(B9), pp.18159-18173.

32. Rice, J. R., Sammis, C. G. & Parsons, R. 2005 Off-fault secondary failure induced by a dynamic slip pulse. *Bull. Seismol. Soc. Am.* **95**, 109–134. (doi:10.1785/0120030166)

33. Andrews, D. J. 2005 Rupture dynamics with energy loss outside the slip zone. *J. Geophys. Res. B Solid Earth* **110**, 1–14. (doi:10.1029/2004JB003191)

34. Doan, M. L. & D'Hour, V. 2012 Effect of initial damage on rock pulverization along faults. *J. Struct. Geol.* **45**, 113–124. (doi:10.1016/j.jsg.2012.05.006)

35. Han, R., Shimamoto, T., Hirose, T., Ree, J.H. and Ando, J.I., 2007. Ultralow friction of carbonate faults caused by thermal decomposition. *Science*, *316*(5826), pp.878-881.

36. Di Toro, G., Han, R., Hirose, T., De Paola, N., Nielsen, S., Mizoguchi, K., Ferri, F., Cocco, M. & Shimamoto, T. 2011 Fault lubrication during earthquakes. *Nature* **471**, 494–498. (doi:10.1038/nature09838)

37. Togo, T. and Shimamoto, T., 2012. Energy partition for grain crushing in quartz gouge during subseismic to seismic fault motion: an experimental study. *Journal of Structural Geology*, *38*, pp.139-155.

38. Lyakhovsky, V., Sagy, A., Boneh, Y. and Reches, Z.E., 2014. Fault wear by damage evolution during steady-state slip. *Pure and Applied Geophysics*, *171*(11), pp.3143-3157.

39. Savage, H. M. & Brodsky, E. E. 2011 Collateral damage: Evolution with displacement of fracture distribution and secondary fault strands in fault damage zones. *J. Geophys. Res.* **116**, B03405. (doi:10.1029/2010JB007665)

40. Lundberg, B. 1976 A Split Hopkinson Bar Study of Energy Absorption in Dynamic. *Int. J. Rock Mech. Min. Sci. Geomech. Abstr.* **13**, 187–197. (doi:10.1016/0148-9062(76)91285-7)

41. Ravi-Chandar, K. & Yang, B. 1997 On the role of microcracks in the dynamic fracture of brittle materials. *J. Mech. Phys. Solids* **45**, 535–563. (doi:10.1016/S0022-5096(96)00096-8)

42. Zhang, Z. X., Kou, S. Q., Yu, J., Yu, Y., Jiang, L. G. & Lindqvist, P. A. 1999 Effects of loading rate on rock fracture. *Int. J. Rock Mech. Min. Sci.* **36**, 597–611. (doi:10.1016/S0148-9062(99)00031-5)

43. Xia, K., Nasseri, M. H. B., Mohanty, B., Lu, F., Chen, R. & Luo, S. N. 2008 Effects of microstructures on dynamic compression of Barre granite. *Int. J. Rock Mech. Min. Sci.* **45**, 879–887. (doi:10.1016/j.ijrmms.2007.09.013)

44. Kolsky, H. 1949 An Investigation of the Mechanical Properties of Materials at very High Rates of Loading. *Proc. Phys. Soc. Sect. B* **62**, 676–700. (doi:10.1088/0370-1301/62/11/302)

45. Chen, W. W. & Song, B. 2013 *Split Hopkinson (Kolsky) Bar*. (doi:10.1017/CBO9781107415324.004)

46. Li, X.B., Lok, T.S., Zhao, J. and Zhao, P.J., 2000. Oscillation elimination in the Hopkinson bar apparatus and resultant complete dynamic stress–strain curves for rocks. *International Journal of Rock Mechanics and Mining Sciences*, *37*(7), pp.1055-1060.

47. Davies, E.D.H. and Hunter, S.C., 1963. The dynamic compression testing of solids by the method of the split Hopkinson pressure bar. *Journal of the Mechanics and Physics of Solids*, *11*(3), pp.155-179.

48. Brunauer, S., Emmett, P. H. & Teller, E. 1938 Adsorption of Gases in Multimolecular Layers. *J. Am. Chem. Soc.* **60**, 309–319. (doi:citeulike-article-id:4074706\rdoi: 10.1021/ja01269a023)

49. Gregg, S.J., Sing, K.S.W., 1982. Adsorption, Surface Area and Porosity, second ed.

50. Academic Press. 313pp.

51. Yoshioka, N., 1986. Fracture energy and the variation of gouge and surface roughness during frictional sliding of rocks. *Journal of Physics of the Earth*, *34*(4), pp.335-355.

CHAPTER 2

EXPERIMENTAL CONSTRAINTS ON DYNAMIC PULVERIZATION AS A DISSIPATIVE PROCESS DURING SEISMIC SLIP

Troy J. Barber and W. Ashley Griffith, University of Texas at Arlington, Arlington, TX, USA.

This manuscript was submitted for publication in the special issue of *Philosophical Transactions of the Royal Society A* concerning "Faulting, friction and weakening: from slow to fast motion" in 2016.

Abstract

Various fault damage fabrics, from gouge in the principal slip zone, to fragmented and pulverized rocks in the fault damage zone, have been attributed to brittle deformation at high strain rates during earthquake rupture. These fault zone fabrics are significant in terms of 1) the information they contain about coseismic deformation mechanisms, 2) the role they play in dissipating energy and contributing to slip weakening during earthquake rupture, and 3) their influence on fault rock mechanical and hydraulic properties. Past experimental work has shown that there exists a critical threshold in stress-strain rate space through which rock failure transitions from failure along a few discrete fracture planes to pulverization. We present new experimental results on Arkansas Novaculite and Westerly Granite in which we quantify fracture surface area produced by pulverization and examine the controls of pre-existing mineral anisotropy on dissipative processes at the microscale. The results have important implications for the partitioning of dissipated energy under extreme loading conditions expected during earthquakes and the scaling of high speed laboratory rock mechanics experiments to natural fault zones.

Key Words

Faulting, dynamic rupture, pulverization, frictional weakening, fracture energy

Introduction and Background

Introduction

Fault damage zones are the manifestation of numerous processes acting on faults throughout the seismic cycle [1]. Damage may be largely the result of pre-existing anisotropy [2]; it may form in the process zone of propagating cracks and slip pulses [3–5], or at geometric barriers or step overs along discontinuous faults [6,7]; or it may

result from dynamic, transient loading during fast earthquake rupture [8–10]. Intense grain-size reduction via fragmentation and pulverization in the latter dynamic loading scenario has been shown experimentally to correspond with rapid weakening during the initial stage of unstable frictional slip, and likely contributes to fault instability [11,12]), Some have conjectured that the production of fine grained gouge may also constitute a major energy sink within the principal slip zone (psz) during the rupture process [8,13,14], although this conclusion is debated [15].

Recent work has attributed an apparent break in scaling between breakdown work in high speed rock friction tests to fracture energy from seismological records of earthquakes. In particular Nielsen et al. [16] showed that the fracture energy calculated as the work done during the frictional weakening process in rotary shear tests (G_f) closely corresponds to the seismologically determined fracture energy from natural earthquakes (G') for events with slip between 1 cm and 1 m ($\sim 3 \leq M_w \leq 7$), but for larger events G_f underestimates G'. They ascribed this discrepancy to energy dissipation due to inelastic off-fault yielding, which is expected to increase with increasing rupture size [16,17]. Therefore, it is possible that the combination of pulverization in the psz and pulverization/dynamic fracture in the damage zone may indeed constitute a significant portion of the energy dissipated during large earthquakes.

The brittle damage process in rocks exhibits a strain rate dependence, passing through a critical high strain rate transition [18,19]. At lower strain rates macroscopic failure is achieved via localized, through-going fractures, whereas high strain rates lead to pervasive, intersecting fractures and, eventually, bulk failure through intense fragmentation. This has led a number of workers to interpret pulverized rocks in fault damage zones as products of dynamic rupture propagation approaching, or in some cases exceeding, the shear wave speed [18–22]. Whereas past experimental work had

delineated critical strain rate and stress thresholds for the pulverization transition, the physical mechanisms for pulverization, particularly as they affect earthquake propagation and frictional slip are less-well understood. In extending our understanding of the fragmentation and pulverization process in rocks beyond simply recognizing the products of dynamic rupture in the rock record [23], and the feedbacks between fragmentation and earthquake rupture, it is necessary to develop a well-constrained model of fragmentation mechanics, including the relationship between load history and the degree of fragmentation, and the dissipated energy involved in this fragmentation. Here we take a step in this direction by studying the effect of the complete load path on the pulverization transition, as well as the degree of comminution that occurs across this transition with particular focus on the energy sink represented by this process. We also explore the role of pulverization in frictional weakening, as well as the challenge of scaling these experimental results to natural fault rocks.

Field Observations of Pulverized Fault Zone Rocks

In nature, the fragmentation transition is evidenced by intensely comminuted rocks that are associated with fast strain-rate events like large earthquake rupture, explosive volcanic eruption, and bolide impact, as well as events related to mining, military, and excavation activities such as rock burst and explosive blasting. Under such extreme loading conditions, rocks spanning a wide range in composition and grain size are often reduced to submicron sized fragments, even when subjected to small total strain [14,15,24]. Wilson et al. [14] found that fault gouge from two fault zones which were disparate both in terms of slip history and host rock mineralogy exhibited very similar particle size distribution (PSD), suggesting that earthquake rupture dynamics, and not cumulative slip wear, governed the formation of the gouge material. Reches and

Dewers [8] suggested that transient changes in volume associated with stress and strain rate amplification near the tip of fast propagating earthquake ruptures served as a pulverizing mechanism for producing the reduced particle size typical of fault gouge.

The recent identification of wide swaths (10s to 100s of meters) of pulverized fault zone rocks (PFZR) that appear to have been shattered *in-situ* has further muddied the water surrounding coseismic brittle damage processes. The texture and damage distribution of PFZR distinctly differ from the breccias and cataclasites characteristic of most fault damage zones. Microstructurally, PFZR exhibit profuse and dense networks of microcracks. Grain size is pervasively reduced, often to the nanometric scale, while original rock fabrics and microstructures are recognizably preserved [14,15,25,26]. At the fault scale, pulverized rocks appear to be limited to shallow crustal depths and often exhibit an asymmetric damage pattern about the fault plane, preferring formation in the *stiffer* fault blocks [15,27–29].

Several outstanding questions with regard to pulverized fault rocks include: 1) How much energy is consumed in producing the extensive fracture surface area indicative of pulverized rocks, and how is that energy distributed over multiple seismic cycles? Consensus indicates that the portion of the dissipated energy during earthquakes consumed in creating fracture surfaces is ~1% [15,25,30], but some studies indicate that this work is as great as 50% [8,14]. 2) What micromechanical processes contribute to the intense comminution evident in pulverized rocks? Commercial crushing and grinding operations [31] as well as lab and field studies of rock deformation [24] indicate the existence of a mineral-specific, minimum possible grain size attainable via fracture under quasi-static compressive loading (i.e. a grind limit), a result supported by fragmentation models [32,33]. However, tensile loading or compressive loading at very high (approaching shock) strain rates *may* produce further comminution [33]. 3)

Beyond critical stress and strain rate thresholds, what aspects of loading history govern the transition to rock pulverization, and what can these controls reveal about the rupture and slip processes on natural faults which contribute to their formation and, more importantly, to frictional weakening processes during earthquakes?

Rock Pulverization in the Lab

Experimental studies of rock fragmentation have been conducted primarily using the Split Hopkinson Pressure Bar (SHPB), a device by which rock samples are loaded by a dynamic uniaxial compressive pulse under strain rates between 10^1 and 10^3 s^{-1} [34]. Motivated by the observations of pulverized rocks along the San Andreas Fault (SAF) zone near Tejon Pass, CA [14,15,26,29], Doan and Gary [18] performed SHPB experiments on specimens of Tejon Lookout granite collected from just outside the heavily pulverized damage zone. They showed that the transition from failure along a few discrete fracture planes to pulverization occurs in Tejon Lookout granite beyond a critical strain rate threshold of ~150 s^{-1}. To study the effect that any preexisting damage may have had on the tests, they conducted similar experiments on Tarn granite, a relatively undamaged rock, and found an increase in the critical strain rate of transition to pulverization (~250 s^{-1}). Doan and d'Hour [35] showed that the data agree with statistical theories for fracture propagation, wherein the rate-dependent brittle response of the material depends on the preexisting flaw density and length distribution within the specimen. They suggest that pulverization in nature is a feedback process, wherein a rock sustains cumulative profuse microcrack damage from each successive high strain rate loading event, which, in turn, reduces the strain rate threshold of pulverization for the next event. Therefore, pulverized rocks may be considered a marker of repeated high strain rate loading events, a conclusion reinforced by subsequent work [36]. Experiments accounting for the effects of burial depth by encasing rock specimens in

confinement collars have also shown that initially undamaged Westerly granite consistently transitioned to pulverization at strain rates of ~250 s^{-1}, and that this threshold increases with increasing confining pressure [19].

Correspondence between fast loading rate, strength/energy consumption increase, and increase in fracture surface area created during SHPB tests has been recognized and documented qualitatively using optical and scanning electron microscopy [37–40]. However, in the geologic literature very few efforts to directly measure the energy partitioned into fracture growth during dynamic loading of rocks have been documented, and published data on the degree of fragmentation in laboratory and natural settings are few. Moreover, the focus is often placed on the final wear product, without regard to differentiating fragments formed through distinct deformation mechanisms. Keulen et al. [24] suggested that grain size reduction in fault zones develops via two distinct mechanical processes: pulverization is induced during initial rupture and continued, lower-strain rate comminution into gouge occurs through grinding wear and shear processes during subsequent slip. They argued that changes in the dominant mechanism of comminution are reflected in particle morphology and size distribution. High speed friction experiments commonly yield nanoparticles [41] exhibiting a specific surface area in one case of ~ 16 m^2/g [11], although it is unclear how much of this grain size reduction is caused by mechanical pulverization during the initial acceleration phase of slip vs. abrasive wear or chemical reactions during shearing. Brunauer-Emmett-Teller (BET) surface area analysis of fresh gouge collected from a recently-exposed shear fracture in quartzite with small net slip yielded a specific surface area of ~0.7 m^2/g [13].

Methods

Specimen selection and preparation

We focus on two rock types in this study: Arkansas Novaculite (AN) and Westerly Granite (WG). AN is a compositionally homogeneous, minimally porous (<<1%), and mechanically isotropic quartz rock, which is virtually flaw-free above the grain scale (5-10 μm). As such, AN is an ideal analog and well suited for evaluating continuum-based micromechanical models of brittle failure in rocks. WG is polymineralic (27% quartz, 66% feldspars, 5% micas, 2% accessory minerals; [42]), coarser grained (~750μm), and mechanically isotropic at the hand-sample scale. It was selected as a well-studied counterpart which is more representative of the continental crust. Specimens were cored into cylinders and faces were machined perpendicular to the axial direction to a tolerance of 0.025 mm. In this study, we work with two specimen dimensions: L/D = ~12mm/25mm = ~0.5 and L/D = ~15mm/15mm = ~1.0, both within the recommended range of slenderness ratios [43].

Experimental Procedure

The SHPB consists of a loading apparatus and a system for monitoring mechanical response. The loading apparatus used in this study (Figure 2-1) is composed of a compressed gas gun and three 38.1 mm diameter C-250 maraging steel bars (striker bar, incident bar, transmitted bar; Fig 1) of density, ρ_b = 8.054 g/cm^3, and Young's modulus, E_b = 185 GPa. The length of the incident and transmitted bars is 2370 mm, and the striker bars are 229mm and 305mm long. Signals from two strategically placed metallic foil-type strain gages are treated by a signal conditioning amplifier and digitally recorded using a high speed oscilloscope. The SHPB operates by firing the striker bar, the velocity of which is monitored with optical sensors located on the gun barrel. The striker impacts the incident bar, generating a compressive wave (incident pulse) that travels along the incident bar toward the cylindrical specimen sandwiched between the

incident and transmitted bars. Striker bar length controls the load duration experienced by the specimen, and varying the striker bar impact speed changes the loading rate and stress amplitude. Upon reaching the specimen, part of the wave energy (reflected pulse) is reflected from the incident bar/specimen interface back along the incident bar. The remaining wave energy (transmitted pulse) is transmitted through the specimen/transmission bar interface and absorbed by a bar stop at the end of the transmission bar. The strain gauges record the incident, reflected, and transmitted waves, which Kolsky [44] showed can be related to the instantaneous stress, strain, and strain rate in the specimen as long as dynamic force equilibrium is maintained on both of the specimen faces during loading (See Supplementary Methods for details). In the SHPB configuration used in this study, a momentum trap mounted on the incident bar prevents the sample from being loaded by multiple reflections of the incident wave, thereby limiting the sample to a single loading pulse.

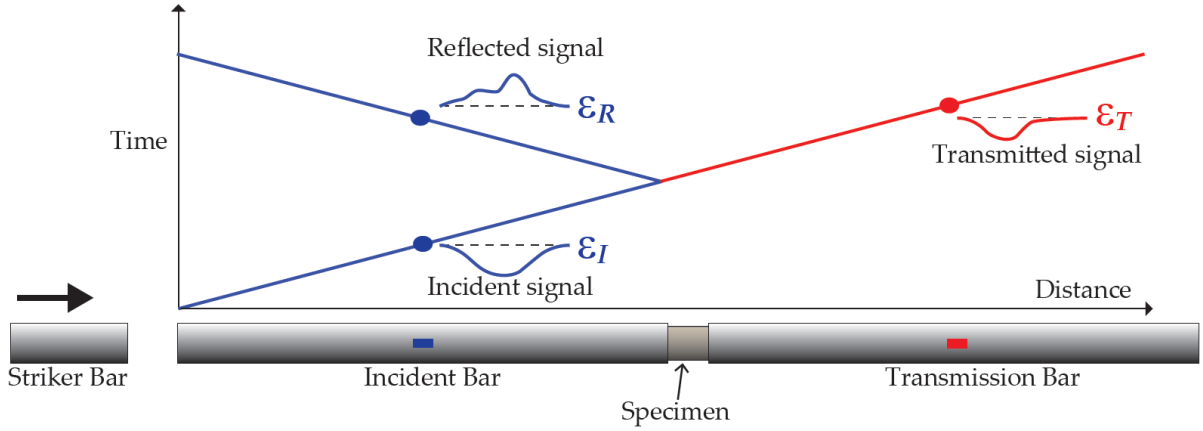

Figure 2-1. Conceptual diagram of a compressive SHPB system depicting the loading apparatus and associated wave travel time-distance plot

Energy Budget

The energy carried by an elastic wave during a SHPB experiment can be represented as

$$W = \left(\frac{1}{2}\rho_b A_b C_b^3 + \frac{1}{2}A_b C_b E_b\right)\int_0^t \varepsilon_b^2(t)\,dt \quad (1)$$

where ρ_b is the density of the bar material and $\varepsilon_b(t)$ is the instantaneous strain measured in the bar [45]. The total energy consumed in damaging the specimen, W_d, is

$$W_d = W_I - W_R - W_T \quad (2)$$

where W_I, W_R, W_T represent the energy carried by the incident, reflected, and transmitted waves, respectively. The total incident wave energy W_I increases predictably with the product of striker bar length and shot velocity. Generally, total dissipated energy W_d increases both in absolute magnitude and as a percentage of the total system energy with increasing qualitative damage state. The energy consumed in damaging the specimen can be further partitioned into energy used to create new fracture surfaces or *fracture surface energy*, W_f, kinetic energy of fragments after failure, W_k, and any other energy sinks in the system, W_0. The fracture surface energy is related to the other work budget terms by:

$$W_f + W_k + W_0 = W_I - W_R - W_T \quad (3)$$

In order to characterize W_f, we examine select post-mortem specimens by mechanical sieving, BET analysis of specific surface area, and scanning electron microscopy.

Post-mortem damage characterization

All specimens are classified as intact, split/fragmented, or pulverized (Figure 2-2) based on a qualitative characterization of damage state [18,19,46]. We selected a few

pulverized post-mortem specimens for measurement of newly created surface area using gas adsorption following the BET method [47], which considers the quantity of adsorbate gas molecules of effective surface area, A_m, adsorbed onto the accessible surfaces of an adsorbent material. Adsorbed gas is assumed to form a monolayer at very low pressure and the adsorbed quantity is modeled as a function of gas pressure and temperature. Another common practice is to estimate collective particle surface area using size distributions [14,15,48]. Popular tools used for measuring particle size such as Coulter counters and mechanical sieves tend to size particles according to their smallest dimension, but give no information on particle shape, leading to an underestimation of surface area [13]. This necessitates the assumption of some representative surface roughness to bring about more accurate estimates of real particle surface area. Gas adsorption offers an advantage over estimates of new crack surface area based on simple particle size analysis in that gases can account directly for surface roughness and penetrate into cracks intersecting particle surfaces.

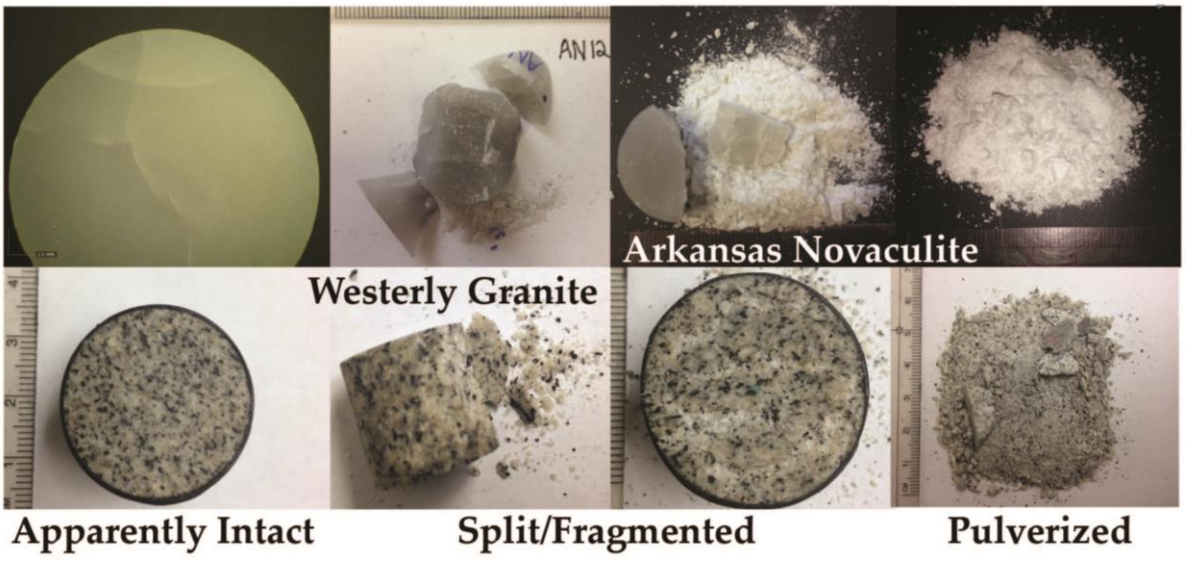

Figure 2-2. Qualitative classification of post mortem specimen damage for AN and WG tests.

Select specimens were mechanically dry sieved for two minutes into size fractions bounded by 0.0, 0.063, 0.125, 0.250, 0.5, 1.0, 2.0, and > 2.0 mm. All subsamples were outgassed for 3 hrs. at 200°C prior to analysis and the adsorptive gas used in this study was Kr. Scanning electron micrographs of specimen fragments were used to describe particle surface morphology and to further delineate particle size distributions beyond the resolution of sieve size bins. The BET measured specific surface area, *SSA* (i.e., surface area per unit mass), of different size fractions for an individual specimen were measured and summed to yield the total particulate surface area for that specimen. Fracture surface area measurements are used to calculate equated estimates of the portion of energy dissipated in the creation of new surface area during a single pulverization event.

To further explore the effect of comminution mechanism on fragment morphology and surface area, BET surface area measurements and scanning electron microscopy were performed on hand-ground specimens as well. Undamaged samples of AN and WG were sectioned into thin slivers using a low speed diamond saw to minimize internal deformation. The resulting slivers were then slowly hand-ground using a steel mortar and pestle. Sieving and gas adsorption were conducted on ground specimens according to the same procedure as the dynamically pulverized specimens.

Results

Mechanical results

Due to the high uniaxial compressive strength (UCS) of AN, bringing the rock to failure at low strain rates with the SHPB used in this study posed a challenge. As such, very few specimens were brought to failure via localized, through going fracture. Dynamic UCS of AN ranges from about 1.0 ~ 1.3 GPa at strain rates of 130 ~ 170 s^{-1} to about 1.65 ~ 1.80 GPa at strain rates of 250 ~ 580 s^{-1} (Figure 2-3A, 4A). Dynamic UCS of WG (Figure 2-3B,4B) ranges from about 280 ~ 375 MPa at strain rates of 150 ~ 900 s^{-1}. With the exception of one of the WG tests, the profile of the stress versus strain curve predicted the qualitative damage state for both AN and WG tests, with apparently intact specimens elastically unloading with a slope similar to that of the loading portion of the curve, split/fragmented specimens unloading but retaining permanent strain, and pulverized specimens completely losing their load bearing capacity (Figure 2-3).

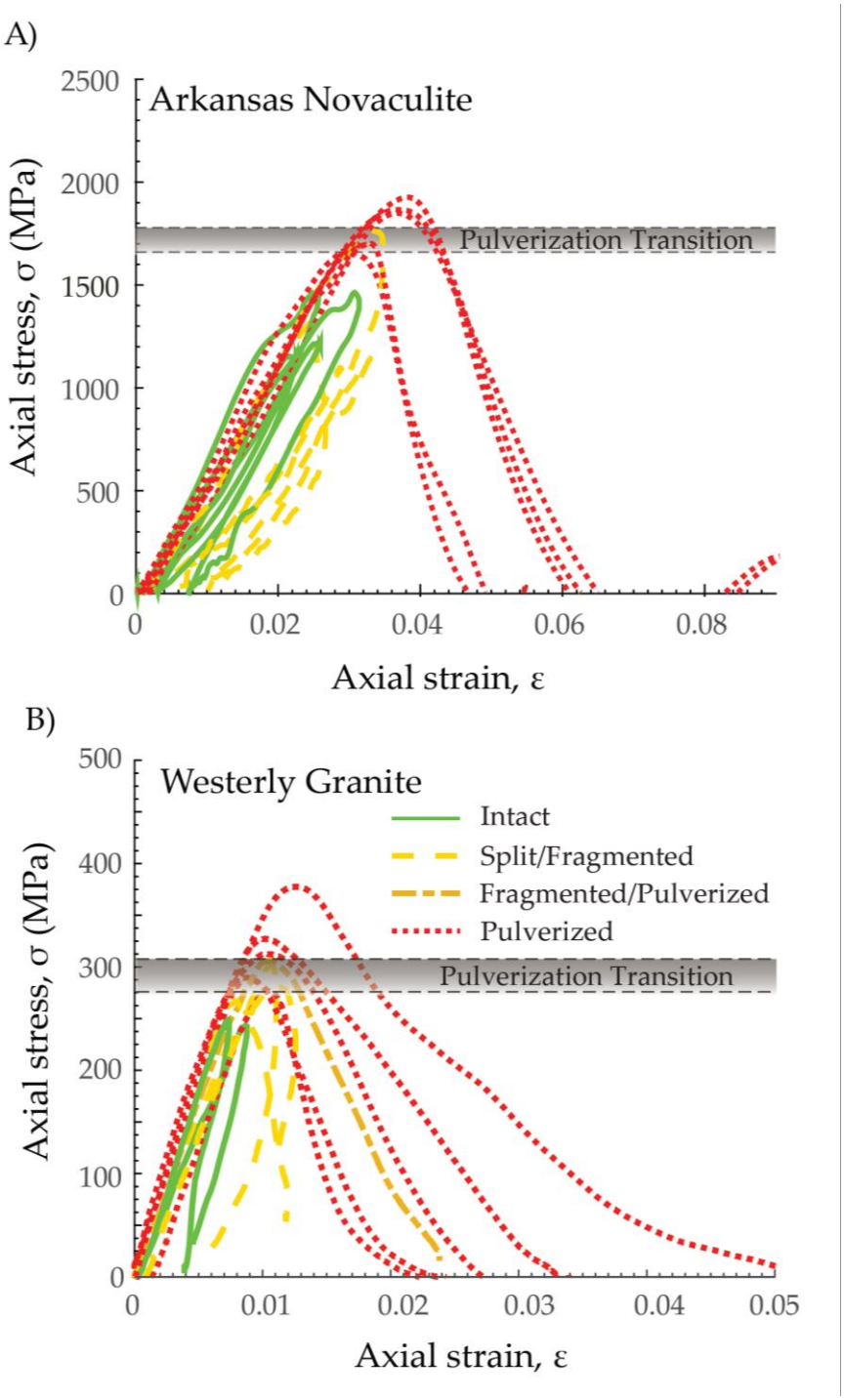

Figure 2-3. Axial stress versus axial strain curves for SHPB tests on A) AN and B) WG. Note that one WG specimen was classified as fragmented/pulverized (marked by the tan colored, dash-dot curve). This specimen fragmented into several large fragments, each of which contained pervasive microfracture, and the specimen lost all load bearing capacity. We, therefore, interpret this specimen to best mark the end of transition to pulverization in WG.

Previous SHPB studies of dynamic pulverization have shown that peak stress and strain rate delineate the transition to pulverization [18,19,36]. For our tests on AN, the relationship between failure mode, peak stress, and strain rate appears less clear. While all pulverized samples failed at stresses > 1600 MPa and strain rates > 400 s^{-1}, several specimens that failed via discrete fracture did so at lower peak stresses and strain rates than other specimens which remained apparently intact (Figure 2-4). Consistently, this occurred for tests with longer pulse duration. Conversely, pulverization only occurred for pulse durations < 160 μs. For a complete summary of SHPB experimental conditions and mechanical results, see Supplementary Tables S1 and S2.

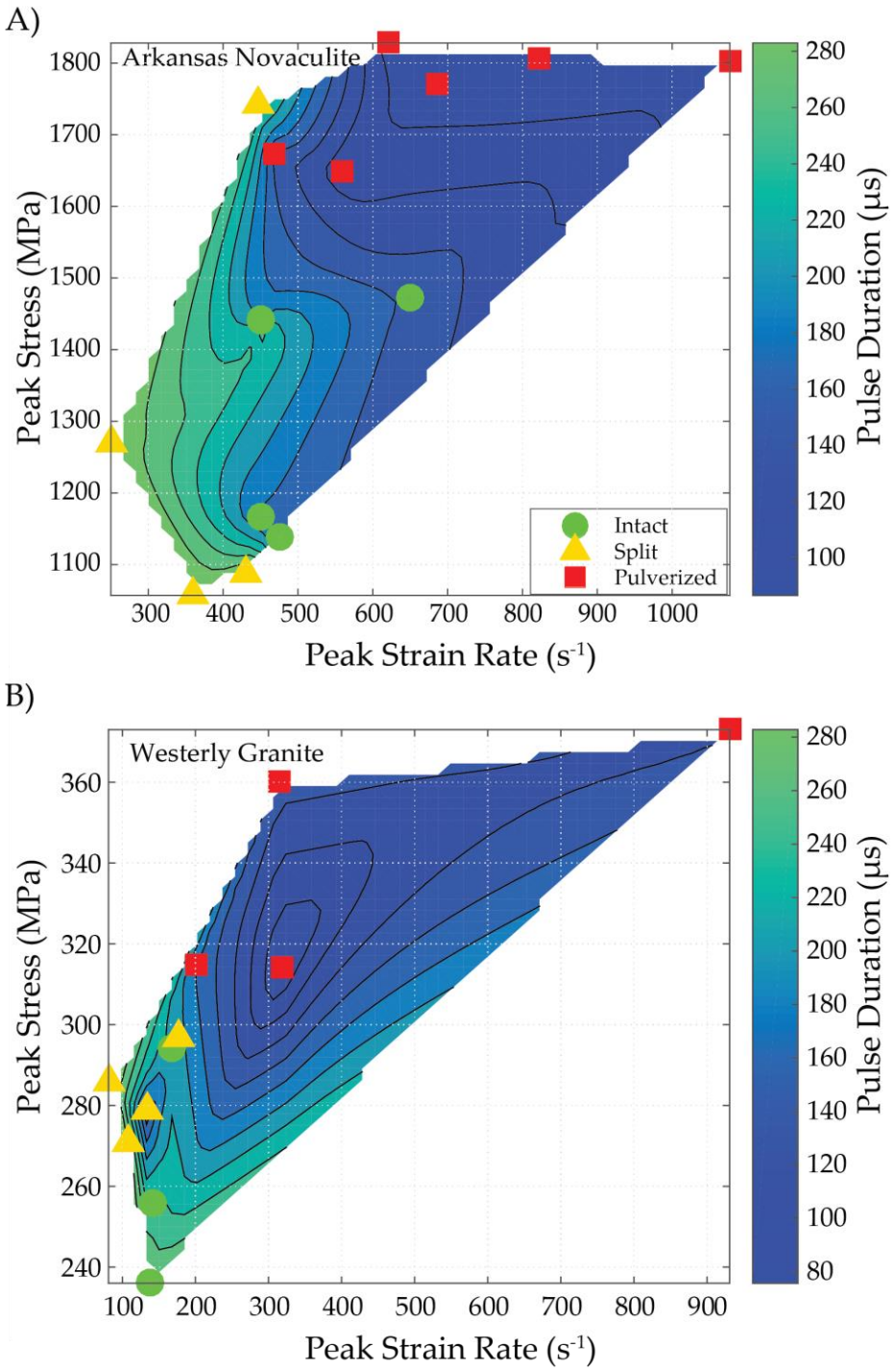

Figure 2-4. Peak stress versus peak strain rate experienced prior to failure shown with contours of incident pulse duration for A) AN and B) WG specimens loaded with the SHPB. Green circles, yellow triangles, and red squares represent specimens classified as intact, split/fragmented, and pulverized, respectively.

Post mortem damage characterization

In order to characterize W_t, we examine select post-mortem specimens by mechanical sieving, BET analysis of specific surface area, and scanning electron microscopy. In order to generate enough material in the smallest size fraction for gas adsorption analysis, hand-ground particles often underwent multiple cycles of sieving and grinding until sufficient fine material was generated. Because of the bias imparted by this crushing procedure, no meaningful relationship should exist between the mass of each hand-ground size fraction and the initial mass of intact material. Thus, the particle size distribution (PSD) was not measured for hand-ground specimens. The PSD of all the pulverized AN specimens is comparable, as a first order approximation, with the mass majority of particles falling between 0.063 and 2.0 mm (Figure 2-5). In contrast, the PSD of pulverized WG specimens are consistently positively skewed, showing a particularly larger mass percentage of particles greater than 2 mm. BET specific surface area (SSA) measurements were performed on individual size fractions from a total of five (one hand-ground and four pulverized) AN specimens and two (one hand-ground and one pulverized) WG specimens (Figure 2-6). For an ideal sphere of density, ρ, geometric specific surface area, SSA_{ideal}, scales linearly with particle radius, r, as

$$SSA_{ideal} = 3(\rho r)^{-1} \quad (4)$$

Introducing a roughness factor, λ, accounts for real deviations from ideal spherical geometry, where λ is typically defined as the ratio of surface area of a real particle to that of an ideal sphere. Considering that all real rocks contain internal flaws down to the nanometer scale, the true SSA must also include a term to describe internal surface area of the particle, SSA_{int}, such that

$$SSA = 3\lambda(\rho r)^{-1} + SSA_{int} \quad (5)$$

It is common practice to extrapolate linear fits to plots of SSA versus inverse particle size (r^{-1}) to yield estimates of SSA_{int} [49]. We follow this practice and plot SSA against r^{-1}, such that Eq. (5) plots as a straight line with slope proportional to the average surface roughness, λ, of the particles and vertical intercept equal to SSA_{int} (Figure 2-6). Table 2-1 relates the particle size bins used during sieving to corresponding ranges of r^{-1}.

Table 2-1. Particle size and related inverse radius range

Particle size (mm)	**Inverse radius (mm^{-1})**
2.0 – 1.0	1.0 – 2.0
1.0 – 0.5	2.0 – 4.0
0.5 – 0.25	4.0 – 8.0
0.25 – 0.125	8.0 – 15.9
0.125 – 0.063	15.9 – 31.7
0.063 - 0	> 31.7

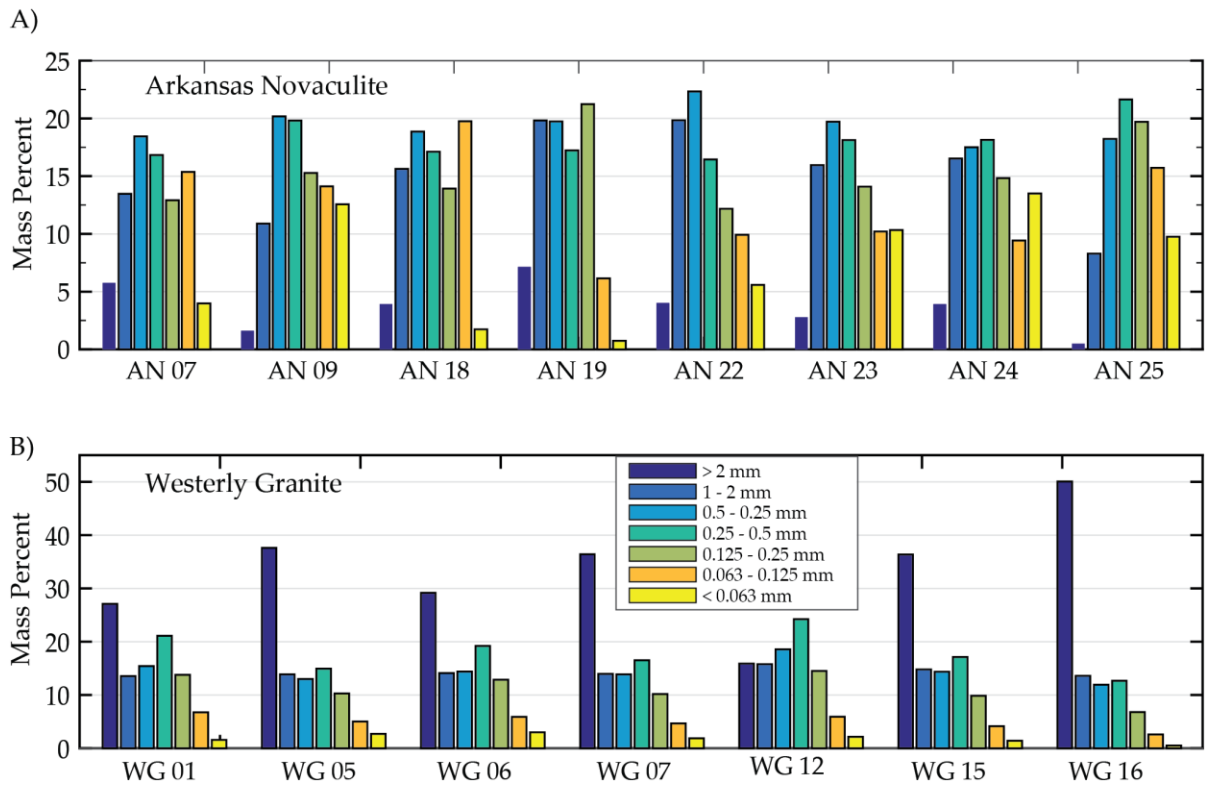

Figure 2-5 . Histograms of particle size distribution by mass percent for dynamically pulverized specimens of A) AN and B) WG.

The *SSA* of both pulverized and hand-ground AN (Figure 2-6A) generally scale inversely with particle size. The values of *SSA* for different particle size bins ranges from 0.0453 – 0.7065 m^2/g for pulverized AN and from 0.0363 – 0.1779 m^2/g for the corresponding hand-ground material. These values are comparable to those reported by Osgaard and Brace [13] for BET surface area measurements made on fresh quartzite fault gouge collected along mining-induced shear fractures. The linear fit to pulverized samples is poor, particularly in the range 10 $mm^{-1} < r^{-1} < 30$ mm^{-1}, where the scatter is large. The slope of the linear fit to pulverized specimens ($\lambda = 8.92$) is large relative to that of the hand-ground samples ($\lambda = 1.94$). As the model suggests, this might be

interpreted as greater particle surface roughness, but also might be caused by a greater sub-fraction of fine (submicron particles) in the pulverized samples not delineated by the sieving process. For specimens AN18 and AN19, insufficient material in the < 63 μm size range was collected to perform BET analysis. Therefore, only for specimens AN07 and AN09 could the surface area from each size fraction be summed to yield the total new fracture surface area created during the experiment. Some previous studies have presented fracture surface area in units of m^2 per cubic meter of pulverized material = [m^{-1}] [24,30]. The weighted average *SSA* measured in experiments AN07 and AN09 was 0.217 and 0.320 m^2/g, respectively, which is equivalent to $5.73x10^5$ and $8.45x10^5$ m^{-1}.

SSA trends in WG (Figure 2-6B) show some key contrasts to trends in AN tests. At smaller r^{-1} values (larger particle sizes) both pulverized and hand-ground specimens show similar *SSA* values, which decrease with r^{-1} up to a point delineated by the r^{-1} = 3.0 ~ 4.0 mm^{-1} inverse particle size, which corresponds closely with the mean grain size of WG (~750 μm). Beyond this delineation (i.e. at smaller particle sizes), *SSA* of pulverized and hand-ground granite specimens generally increase with r^{-1}, but deviate from one another significantly (by a factor of 8 at the smallest particle size range), suggesting a fundamental difference between hand-ground and pulverized granite specimens below a threshold particle size. *SSA* for different particle size bins ranged from 0.0526 – 0.201 m^2/g for pulverized WG and from 0.0730 – 0.904 m^2/g for the corresponding hand-ground material. The weighted average *SSA* measured in experiment WG01 was 0.0762 m^2/g, equivalent to $2.02*10^5$ m^{-1}.

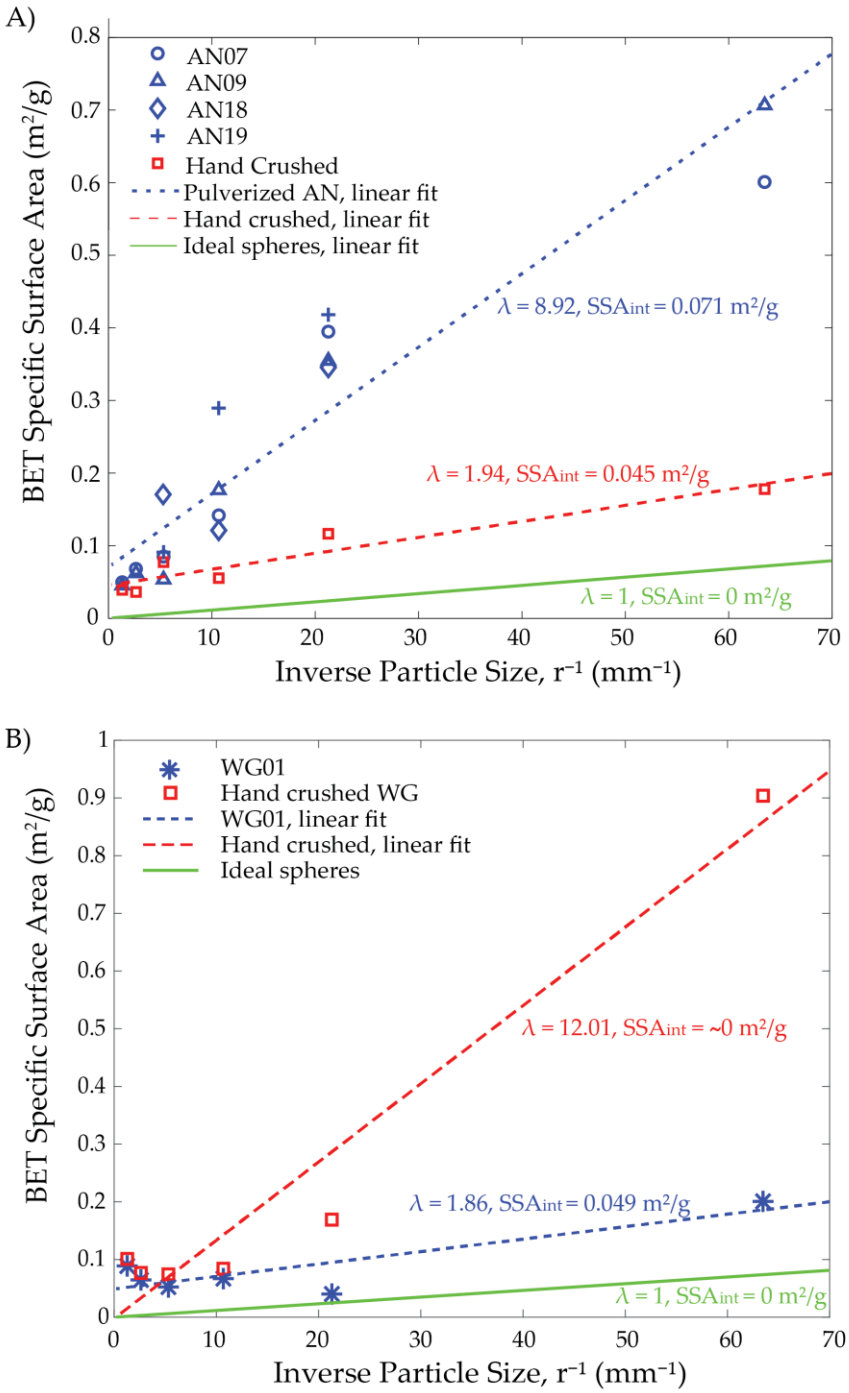

Figure 2-6. BET measured specific surface area (SSA) plotted against the inverse of radius (r^{-1}) on different size fractions of A) AN and B) WG specimens. Blue and red data represent dynamically pulverized and hand-ground specimens, respectively. Linear fits to data are based on Eq. (5), with

model parameters indicated adjacent to each curve. Green curve represents geometric surface area of ideal spheres.

Table 2-2 summarizes the fracture surface energy analysis for specimens AN07, AN09, and WG01. Assuming a specific surface energy of 1 J/m^2 for quartz [50], we used pulverized specimen SSA to calculate the energy dissipated in brittle fracture, W_f, during a single pulverization event. When a rock fails via pulverization, the resulting fragments explode outward with substantial kinetic energy and capturing all of the particles proves difficult, especially for the smallest particles generated, which are powders. For tests on WG, between 98 ~ 99 % of the original specimen mass was collected. However, for tests on AN, which generates substantial amounts of fine particles upon pulverization, capture efficiency was between 82 and 94%. If we consider that the lost particles were as fine as or finer than the smallest fragments observed (0.5-1.0 μm) we can extrapolate the linear fit for the pulverized data in Figure 2-6A out to r^{-1} values equivalent to particle diameters of 1.0 and 0.5 μm. These calculations indicate that AN specimens dissipated a substantially larger portion of energy (10 - 40%) in creating new fracture surface area than WG (~5%), likely owing to the significant contribution of the finest particles.

Table 2-2. Summary of fracture surface energy analysis

Sample ID	Sample Mass (g)	% Mass Collected	Avg BET SSA (m^2/g)	Total SA (m^2)	W_I (J)	W_d (J)	W_f (J)	W_f/W_d
AN07	15.38	87.26	2.90 - 5.65	44.6 – 86.9	1461	433	44.6 – 86.9	0.10 – 0.20

AN09	15.26	83.36	4.02 – 7.83	61.3 – 119.5	1186	268	61.3 – 119.5	0.22 – 0.45
WG01	15.76	98.41	0.076	1.90	215	51	1.90	0.04

Direct microstructural observations of the post-mortem specimens yield some important insights into the micromechanical processes responsible for fragmentation, and these processes vary systematically with loading rate, loading configuration, and lithology. In AN, microcracking occurs well below the pulverization threshold, and, indeed, well-below the macroscopic strength of the rock (Figure 2-7B). In these cases, cracks are opening mode and align with the direction of the axial load. For specimens pulverized using the SHPB, individual fragments span several orders of magnitude in size, but abundant submicron particles are produced, far below the grain size of undeformed AN, attesting to the importance of intragranular fracturing in addition to grain-boundary and intergranular fracture (Figure 2-7C,D). In some cases, intergranular fractures cut across otherwise undeformed grains (Figure 2-7E,F). Fragment surfaces are characterized by conchoidal fracture and twist hackle (Figure 2-7F), and partially coated by submicron particles. The predominance of this texture attests to the important role of mixed Mode I-III fracture propagation, likely due to interaction between adjacent propagating microcracks as the sample approaches the pulverization state. The smallest abundant particle size for both pulverized and hand-ground AN is approximately 3-10μm, each particle corresponding to individual quartz grains, and submicron particles appear present in roughly the same amounts (Figure 2-7G,H).

Post-mortem specimens of pulverized and hand-ground WG display some key differences compared to AN. In general, individual particles are less-equant than AN, perhaps owing to the heterogeneous mineralogy, as the long dimension of individual particles are frequently parallel to an obvious cleavage plane in biotite and feldspar fragments (Figure 2-8A,E). Quartz grains in both pulverized and crushed samples display common joint surface textures, particularly twist hackle, on particles ranging in size from a few to hundreds of microns (Figure 2-8C, D). In pulverized and hand-ground specimens, equant submicron particles coat larger fragments, yet submicron-sized particles appear, qualitatively, to be far more prevalent in hand-ground granite samples (Figure 2-8D) than in hand crushed AN. The hand-ground and, to a lesser degree, the pulverized WG specimens show abundant evidence of shear deformation on cleavage planes (Figure 2-8E,F), most dramatically displayed by smeared biotite grains (Figure 2-8F), and the average particle in the smallest size fraction bin (< 63 μm) is substantially smaller for the hand-ground (Figure 2-8B) than for the dynamically pulverized WG sample (Figure 2-8A).

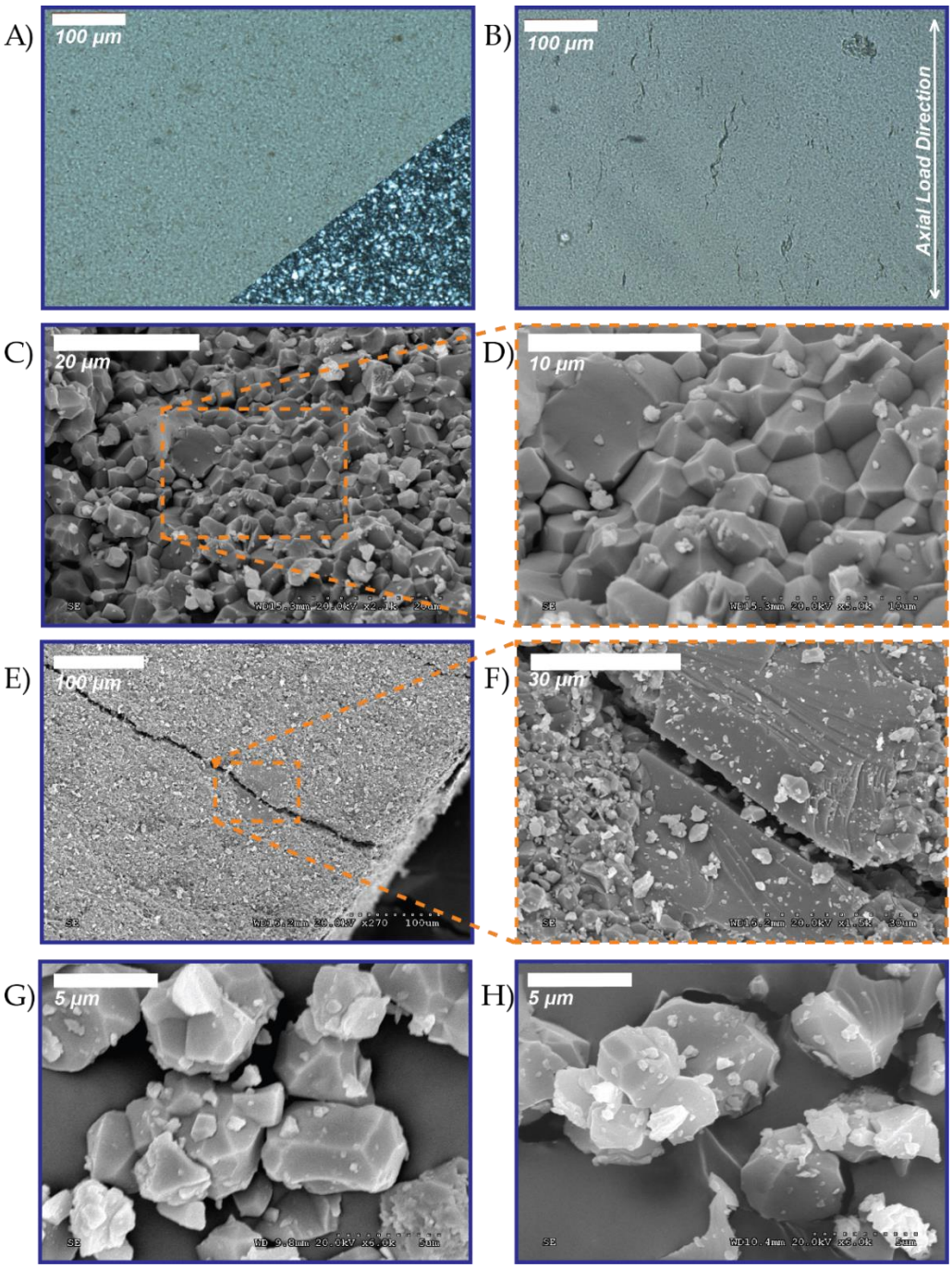

Figure 2-7. Optical light and scanning electron microscope images of AN specimens. A) Plane polarized light (PPL) image of undeformed AN showing absence of flaws above the 5~10 µm grain scale (grains highlighted by crossed polarized (CPL) corner inset). B) PPL image of apparently intact post-mortem specimen after SHPB test showing dynamically grown microcracks parallel to the axial stress direction. C,D) Surface of a dynamically pulverized fragment showing intra- and intergranular cracking features. E,F) Surface of a larger (1-2 mm) fragment showing abnormally large grain cut by

intergranular fracture with twist hackle surface texture. Equant grain scale particles resulting from G) dynamic pulverization and H) hand-grinding.

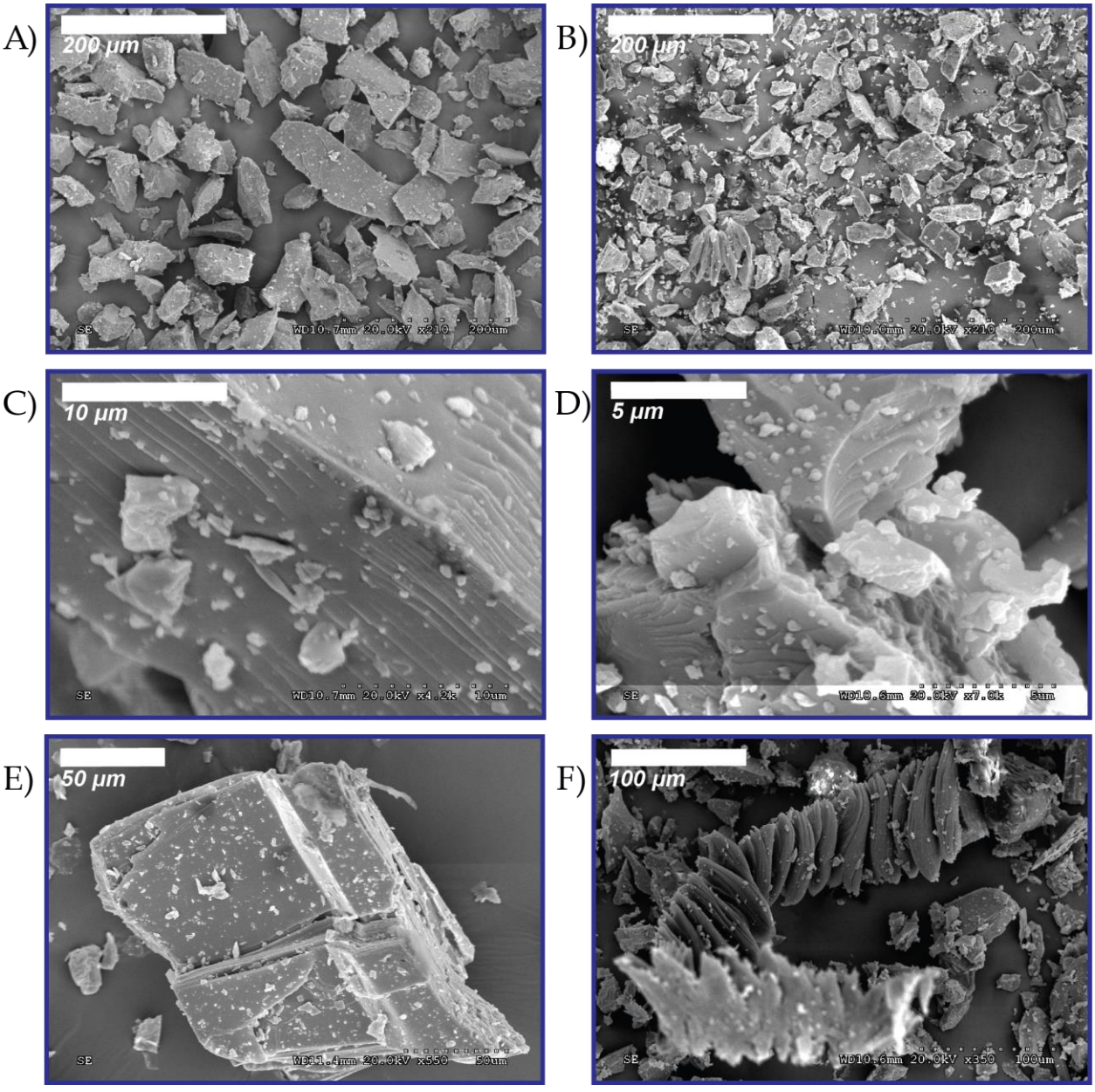

Figure 2-8. Scanning electron microscope images of deformed WG specimens. Fragments from smallest sieve size bin (< 63 µm) are substantially larger for A) pulverized granite than for B) the

corresponding hand-ground specimen. Fracture surfaces exhibiting twist hackle and coated with submicron particles on fragments of both C) pulverized and D) hand-ground granite specimens. Mica grains showing E) substantial surface exposure manifested as opening along grain boundaries and cleavage planes in pulverized WG and F) extraordinary shearing along cleavage planes in hand-ground WG.

Discussion

Fracturing as a component of dissipated energy

Taken together the mechanical data from SHPB experiments, as well as BET SSA data and microstructural observations, provide important insights into the role of material heterogeneity and anisotropy on the pulverization process under compressive loading. The data spread, and resulting non-linear character of the SSA vs. r^{-1} relationship for AN, particularly in the inverse particle size range of $10mm^{-1} < r^{-1} < 30\ mm^{-1}$, is likely a product of the adherence of abundant submicron-sized particles to larger particles (Figure 2-7D, F). Conversely, the non-linearity in the SSA vs. r^{-1} relationship in WG is characterized by a non-intuitive decrease in SSA with increasing r^{-1} in the range $0\ mm^{-1} < r^{-1} < 5\ mm^{-1}$ before increasing with r^{-1} (i.e., with decreasing particle size). It is noteworthy that the average grain diameter of 0.75 mm in WG (r^{-1} =~2.7 mm^{-1}) roughly delineates the change in dependence. The pervasive failure along cleavage planes in micas and feldspars (Figure 2-8B, E, F) exposes new surfaces, whereas this effect is likely under-sampled at successively smaller grain size fractions (increasing r^{-1}) up to the average grain size of the rock. This interpretation is supported by the fact that this trend is repeated for hand-crushed WG samples where shearing along cleavage planes is especially pervasive (Figure 2-8F). Furthermore, the relatively high SSA measurements in the smallest size fraction from hand-ground specimens may be explained by a more finely skewed particle size distribution within this size fraction bin (Figure 2-8B), which is perhaps dominantly generated by the strong activation of shear

deformation (Figure 2-8F) driven by the grinding motion, but facilitated by the natural strength anisotropy of biotite and feldspar minerals. Such shear motion could enhance particle size reduction by wear and localized deformation at the tips of shear cracks, and no such pervasive evidence of shear deformation was observed in either the pulverized or hand-crushed AN samples.

The implied fracture energy associated with the SSA measurements is complicated by a number of factors. First, for experiments AN-07 and AN-09 (and to a lesser extent WG-01), a non-negligible amount of powder was lost, due primarily to escape of fine-sized particulate matter during the experiments; therefore, it is difficult to determine with great certainty the SSA of the missing size fraction. One approach to estimating this missing size fraction is to assume that the smallest size particles observed in the SEM are representative of the lost particles. If, for example, we assume a range of particle sizes of 0.5-1 μm for AN-09, this yields W_f/W_d of 20% to 40%. The WG specimens are more complicated. First, the measured SSA is smaller for pulverized WG, but the total dissipated energy was also smaller, so W_f/W_d is similar to the AN samples. The relatively minor mass percent of fine (i.e. < 63 μm) particles in the pulverized WG samples suggests that the real surface area of the particles may be significantly smaller than those produced during AN experiments. Furthermore, due to the activation of shear on anisotropic grains in WG, it is more difficult to ascribe all of the measured surface area to fracture energy. Instead, shearing on pre-existing planes of weakness likely results in a greater portion of dissipated energy into heat.

It is also worth noting that these results show that uniaxial compression at fast (but finite) strain rates is capable of producing sub-micron particles. This observation suggests that the quasi-static model of a "grind limit" [33] may be a reasonable

idealization for slow deformation rates, but that in the strain rate spectrum of the SHPB (and near the earthquake rupture tip) it is no longer valid.

These experimental observations produce an interesting point of comparison to the theoretical predictions of coseismic temperature rise due to distributed fracture and pulverization in a fault damage zone [51]. Based on stress-strain curves obtained from SHPB experiments on WG under confinement [19], Ben Zion and Sammis [51] estimated the dissipated strain energy available for pulverization and shear heating. Calculating the total surface area created by reducing the original rock volume into 1μm^2 cubes, resulted in an SSA of 2 g/m^2, and the percentage of total work consumed by creation of new fracture surface was small compared to the total dissipated energy; they therefore concluded that nearly all of the dissipated energy goes into shear heating. Our SSA data, which produce roughness constants of $\lambda \approx 9$ for AN and for WG $\lambda \approx 2$, result in SSA of ~1 g/m^2, remarkably similar to the simple thought experiment of [51]. However, given the error introduced to our measurements by the missing abundance of submicron particles, we have shown that the total work invested in fracture may be as great as 40% for AN. Therefore, we may conclude that in relatively homogeneous and undamaged crystalline rocks, temperature rise might be buffered by the creation of fractures, whereas in heterogeneous and heavily pre-fractured media the majority of dissipated energy would be converted to heat.

Implications for faulting, friction, and weakening

This study represents the first quantitative investigation of the amount of dissipated energy partitioned into fracture energy during impulsive compressive loading events on initially intact rocks. And while we cannot yet robustly predict the relationship

between loading parameters and fracture surface area created, our observations provide a number of insights relevant to the role of pulverization in the seismic faulting process.

In particular, it suggests that for several tens of centimeters near the fault where stresses and strain rates exceed pulverization thresholds for common crustal rocks, that rock pulverization can be an effective energy sink to account for a significant portion of dissipated energy, providing a mechanism for the energy sink hypothesized by Nielsen et al. [16]. However, the differences between surface area measurements and microstructural observations of AN and WG suggest that homogeneous continuum models may overestimate the role of mode I fracturing in the pulverization process, and that shearing on pre-existing weak planes may play a larger role. We view the observations in WG as a microscale analog for activation of small damage zone faults and fractures along mature faults [5,52]. The end result of inelastic yielding in the process zone of a propagating rupture is likely intense dynamic fracturing and/or pulverization, but the actual mechanisms might depend on the degree of heterogeneity and existing damage within the damage zone. Furthermore, one might conjecture that, depending on the mode of damage (cracking vs. shearing) the dissipated energy might be variably partitioned into distributed heat, or creation of new fracture surface. Our results indicate that loading conditions relevant to the tip of a propagating earthquake rupture are an effective mechanism for initiating grain size reduction, and as these generally correspond to the particle acceleration phase of a passing rupture [12], this grain size reduction may kick-start rapid weakening due to initial grain size reduction and the exposure of fresh particle surfaces, optimizing the activation of subsequent physico-chemical weakening processes [53]. Our estimates of SSA in dynamically pulverized specimens are an order of magnitude smaller than similar measurements performed on experimentally produced gouge by Reches and Lockner [11]. Based on

our experimental results initial grain size reduction at the tip of a rupture may form the initial stages of weakening, partially confirming the hypothesis of Reches and Dewers [8], but wear processes are necessary to continue the grain size reduction process.

Open Questions

All of the forgoing discussion points are subject to the limitation that the applied loads in the SHPB experiments in this study all consist of smoothly shaped, uniaxial compressive loads with a single cycle of deformation. This results in a scaling challenge on a number of fronts. First, the loading history (including the duration of the applied load) is essential to predicting the brittle yielding behavior. The peak or average stress and strain rate alone do not provide enough information. This conclusion is supported by a recent study which showed that repeated loading cycles at peak stresses and strain rates below the pulverization transition lower the corresponding thresholds for pulverization in rocks [36]. Furthermore, the load history applied to a rock during passage of a dynamic rupture is subject to rapid cycles of loading which, depending on the position relative to the fault (and other complicating factors, e.g., [52]), may vary in amplitude and duration, and also may combine transient pulses of tension and compression [8,52]. Therefore, in order to constrain the constitutive inelastic yielding behavior of rocks due to impulsive loads relevant to earthquake ruptures, future work will need to focus on replicating these more realistic load histories.

Conclusions

We conducted a series of dynamic compression tests on weakly confined AN and WG. The pulverization thresholds for WG, as defined in terms of stress and strain rate, were similar to those found in previous work on unconfined or weakly confined samples [19]. Pulverization thresholds for AN, however, are much higher ($\sigma \approx 1600\ MPa$ and $\dot{\varepsilon} \approx 400 s^{-1}$), but the yield strength at slightly lower strain rates is highly dependent on load duration. Particle size distributions indicate a larger percent of WG rock mass is converted to large fragments, compared to AN. SSA measurements suggest that more of the available energy is invested into creating new fracture surface for AN. Furthermore, dynamic pulverization of AN produces more SSA than the slower process of mechanically grinding, whereas the opposite is true for WG. Microstructural observations indicate that submicron particles are produced in varying amounts for the different experiments, and that mode I cracking, including intergranular fracture, is the dominant grain size reduction in pulverization of AN, whereas exploitation of cleavage planes and minor shearing are also important in WG. Furthermore, SSA measurements for AN, corrected for missing submicron particles, suggest that as much as 40% of dissipated energy in the experiments is invested in the creation of new fracture surfaces. We also discuss the implications of our results on pulverization as a sink of dissipated energy during earthquakes, dynamic weakening of faults at the leading edge of a propagating rupture, and scaling the results of high speed friction and dynamic compression tests to natural fault rocks.

Acknowledgements

This material is based upon work supported in part by the National Science Foundation Graduate Research Fellowship under Grant No. (1144240) and the US Army 737

Research Office under grant number W911NF1410276. The manuscript benefited greatly from discussions with Hamed Ghaffari, Chris Borjas, and Qinhong Hu. We acknowledge Kermit Beird and Merlynd Nestell for their contributions in specimen preparation, as well as Jiechao Jiang, Majie Fan, Elizabeth Griffith, and Samantha Carter for help with microstructural analysis.

References

1. Savage, H. M. & Brodsky, E. E. 2011 Collateral damage: Evolution with displacement of fracture distribution and secondary fault strands in fault damage zones. *J. Geophys. Res.* **116**, B03405. (doi:10.1029/2010JB007665)

2. Davatzes, N. C. & Aydin, A. 2005 Distribution and nature of fault architecture in a layered sandstone and shale sequence: An example from the Moab fault, Utah. *AAPG Mem.* , 153–180. (doi:10.1306/1033722m853134)

3. Delaney, P. T., Pollard, D. D., Ziony, J. I. & McKee, E. H. 1986 Field relations between dikes and joints: Emplacement processes and paleostress analysis. *J. Geophys. Res.* **91**, 4920. (doi:10.1029/JB091iB05p04920)

4. Vermilye, J. M. & Scholz, C. H. 1998 The process zone: A microstructural view of fault growth. *J. Geophys. Res.* **103**, 12223. (doi:10.1029/98JB00957)

5. Savage, H. M. & Cooke, M. L. 2010 Unlocking the effects of friction on fault damage zones. *J. Struct. Geol.* **32**, 1732–1741. (doi:10.1016/j.jsg.2009.08.014)

6. Chester, F. M. & Chester, J. S. 2000 Stress and deformation along wavy frictional faults. *J. Geophys. Res.* **105**, 23421–23430. (doi:10.1029/2000JB900241)

7. Griffith, W. A., Nielsen, S., Di Toro, G. & Smith, S. A. F. 2010 Rough faults, distributed weakening, and off-fault deformation. *J. Geophys. Res.* **115**, B08409. (doi:10.1029/2009JB006925)

8. Reches, Z. & Dewers, T. a. 2005 Gouge formation by dynamic pulverization during earthquake rupture. *Earth Planet. Sci. Lett.* **235**, 361–374. (doi:10.1016/j.epsl.2005.04.009)

9. Griffith, W. A., Rosakis, A., Pollard, D. D. & Ko, C. W. 2009 Dynamic rupture experiments elucidate tensile crack development during propagating earthquake ruptures. *Geology* **37**, 795–798. (doi:10.1130/G30064A.1)

10. Ngo, D., Huang, Y., Rosakis, A., Griffith, W. A. & Pollard, D. 2012 Off-fault tensile cracks: A link between geological fault observations, lab experiments, and dynamic rupture models. *J. Geophys. Res. Solid Earth* **117**. (doi:10.1029/2011JB008577)

11. Reches, Z. & Lockner, D. a 2010 Fault weakening and earthquake instability by powder lubrication. *Nature* **467**, 452–455. (doi:10.1038/nature09348)

12. Chang, J. C., Lockner, D. a. & Reches, Z. 2012 Rapid Acceleration Leads to Rapid Weakening in Earthquake-Like Laboratory Experiments. *Science (80-.).* **338**, 101–105. (doi:10.1126/science.1221195)

13. Olgaard, D. L. & Brace, W. F. 1983 The microstructure of gouge from a mining-induced seismic shear zone. *Int. J. Rock Mech. Min. Sci. Geomech. Abstr.* **20**, 11–19. (doi:10.1016/0148-9062(83)91610-8)

14. Wilson, B., Dewers, T., Reches, Z. & Brune, J. 2005 Particle size and energetics of gouge from earthquake rupture zones. *Nature* **434**, 749–752. (doi:10.1038/nature03433)

15. Rockwell, T., Sisk, M., Girty, G., Dor, O., Wechsler, N. & Ben-Zion, Y. 2009 Chemical and physical characteristics of pulverized tejon lookout granite adjacent to the San Andreas and garlock faults: Implications for earthquake physics. *Pure Appl. Geophys.* **166**, 1725–1746. (doi:10.1007/s00024-009-0514-1)

16. Nielsen, S., Spagnuolo, E., Violay, M., Smith, S. & Di Toro, G. 2016 G : Fracture energy , friction and dissipation in earthquakes. *J. Seismol.* (doi:10.1007/s10950-016-9560-1)

17. Andrews, D. J. 2005 Rupture dynamics with energy loss outside the slip zone. *J. Geophys. Res. B Solid Earth* **110**, 1–14. (doi:10.1029/2004JB003191)

18. Doan, M.-L. & Gary, G. 2009 Rock pulverization at high strain rate near the San Andreas fault. *Nat. Geosci.* **2**, 709–712. (doi:10.1038/ngeo640)

19. Yuan, F., Prakash, V. & Tullis, T. 2011 Origin of pulverized rocks during earthquake fault rupture. *J. Geophys. Res. Solid Earth* **116**, 1–18. (doi:10.1029/2010JB007721)

20. Mitchell, T. M., Ben-Zion, Y. & Shimamoto, T. 2011 Pulverized fault rocks and damage asymmetry along the Arima-Takatsuki Tectonic Line, Japan. *Earth Planet. Sci. Lett.* **308**, 284–297. (doi:10.1016/j.epsl.2011.04.023)

21. Rempe, M., Mitchell, T., Renner, J. J., Nippress, S., Ben-Zion, Y. & Rockwell, T. 2013 Damage and seismic velocity structure of pulverized rocks near the San Andreas Fault. *J. Geophys. Res. Solid Earth* **118**, 2813–2831. (doi:10.1002/jgrb.50184)

22. Fondriest, M., Aretusini, S., Di Toro, G. & Smith, S. A. F. 2015 Fracturing and rock pulverization along an exhumed seismogenic fault zone in dolostones: The Foiana Fault Zone (Southern Alps, Italy). *Tectonophysics* **654**, 56–74. (doi:10.1016/j.tecto.2015.04.015)

23. Rowe, C. D. & Griffith, W. A. 2015 Do faults preserve a record of seismic slip: A second opinion. *J. Struct. Geol.* **78**, 1–26. (doi:10.1016/j.jsg.2015.06.006)

24. Keulen, N., Heilbronner, R., Stünitz, H., Boullier, A.-M. M. & Ito, H. 2007 Grain size distributions of fault rocks: A comparison between experimentally and naturally deformed granitoids. *J. Struct. Geol.* **29**, 1282–1300. (doi:10.1016/j.jsg.2007.04.003)

25. Chester, J. S., Chester, F. M. & Kronenberg, A. K. 2005 Fracture surface energy of the Punchbowl fault, San Andreas system. *Nature* **437**, 133–136. (doi:10.1038/nature03942)

26. Dor, O., Ben-Zion, Y., Rockwell, T. K. & Brune, J. 2006 Pulverized rocks in the Mojave section of the San Andreas Fault Zone. *Earth Planet. Sci. Lett.* **245**, 642–654. (doi:10.1016/j.epsl.2006.03.034)

27. Ben-Zion, Y. & Shi, Z. 2005 Dynamic rupture on a material interface with spontaneous generation of plastic strain in the bulk. *Earth Planet. Sci. Lett.* **236**, 486–496. (doi:10.1016/j.epsl.2005.03.025)

28. Dor, O., Rockwell, T. K., Ben-Zion, Y. & Geophysics, A. 2006 Geological Observations of Damage Asymmetry in the Structure of the San Jacinto, San Andreas and Punchbowl Faults in Southern California: A Possible

Indicator for Preferred Rupture Propagation Direction. *Pure Appl. Geophys.* **163**, 301–349. (doi:10.1007/s00024-005-0023-9)

29. Dor, O., Yildirim, C., Rockwell, T. K., Ben-Zion, Y., Emre, O., Sisk, M. & Duman, T. Y. 2008 Geological and geomorphologic asymmetry across the rupture zones of the 1943 and 1944 earthquakes on the North Anatolian Fault: Possible signals for preferred earthquake propagation direction. *Geophys. J. Int.* **173**, 483–504. (doi:10.1111/j.1365-246X.2008.03709.x)

30. Wechsler, N., Allen, E. E., Rockwell, T. K., Girty, G., Chester, J. S. & Ben-Zion, Y. 2011 Characterization of pulverized granitoids in a shallow core along the San Andreas Fault, Littlerock, CA. *Geophys. J. Int.* **186**, 401–417. (doi:10.1111/j.1365-246X.2011.05059.x)

31. Prasher, C. L. 1987 *Crushing and grinding process handbook*. Wiley. [cited 2016 Mar. 20].

32. Kendall, K. 1979 The impossibility of comminuting small particles by compression. *Nature*. **279**, 169–170. (doi:10.1038/279169d0)

33. Sammis, C. G. & Ben-Zion, Y. 2008 Mechanics of grain-size reduction in fault zones. *J. Geophys. Res.* **113**, B02306. (doi:10.1029/2006JB004892)

34. Xia, K. & Yao, W. 2015 Dynamic rock tests using split Hopkinson (Kolsky) bar system - A review. *J. Rock Mech. Geotech. Eng.* **7**, 27–59. (doi:10.1016/j.jrmge.2014.07.008)

35. Doan, M. L. & D'Hour, V. 2012 Effect of initial damage on rock pulverization along faults. *J. Struct. Geol.* **45**, 113–124. (doi:10.1016/j.jsg.2012.05.006)

36. Aben, F. M., Doan, M.-L., Mitchell, T. M., Toussaint, R., Reuschlé, T., Fondriest, M., Gratier, J.-P. & Renard, F. 2016 Dynamic fracturing by successive coseismic loadings leads to pulverization in active fault zones. *J. Geophys. Res. Solid Earth* , n/a–n/a. (doi:10.1002/2015JB012542)

37. Lundberg, B. 1976 A Split Hopkinson Bar Study of Energy Absorption in Dynamic. *Int. J. Rock Mech. Min. Sci. Geomech. Abstr.* **13**, 187–197. (doi:10.1016/0148-9062(76)91285-7)

38. Ravi-Chandar, K. & Yang, B. 1997 On the role of microcracks in the dynamic fracture of brittle materials. *J. Mech. Phys. Solids* **45**, 535–563. (doi:10.1016/S0022-5096(96)00096-8)

39. Zhang, Z. X., Kou, S. Q., Yu, J., Yu, Y., Jiang, L. G. & Lindqvist, P. A. 1999 Effects of loading rate on rock fracture. *Int. J. Rock Mech. Min. Sci.* **36**, 597–611. (doi:10.1016/S0148-9062(99)00031-5)

40. Xia, K., Nasseri, M. H. B., Mohanty, B., Lu, F., Chen, R. & Luo, S. N. 2008 Effects of microstructures on dynamic compression of Barre granite. *Int. J. Rock Mech. Min. Sci.* **45**, 879–887. (doi:10.1016/j.ijrmms.2007.09.013)

41. Han, R., Shimamoto, T., Hirose, T., Ree, J.-H. & Ando, J.-I. 2007 Ultralow friction of carbonate faults caused by thermal decomposition. *Science* **316**, 878–81. (doi:10.1126/science.1139763)

42. Brace, W. F., Martin, R. J. & Ladanyi, B. 1970 A test of the law of effective stress for crystalline rocks of low porosity. *Int. J. Rock Mech. Min. Sci.* **7**, 123–124. (doi:10.1016/0148-9062(70)90030-6)

43. Dai, F., Huang, S., Xia, K. & Tan, Z. 2010 Some Fundamental Issues in Dynamic Compression and Tension Tests of Rocks Using Split Hopkinson Pressure Bar. *Rock Mech. Rock Eng.* **43**, 657–666. (doi:10.1007/s00603-010-0091-8)

44. Kolsky, H. 1949 An Investigation of the Mechanical Properties of Materials at very High Rates of Loading. *Proc. Phys. Soc. Sect. B* **62**, 676–700. (doi:10.1088/0370-1301/62/11/302)

45. Chen, W. W. & Song, B. 2013 *Split Hopkinson (Kolsky) Bar*. (doi:10.1017/CBO9781107415324.004)

46. Doan, M.-L. L. & Billi, A. 2011 High strain rate damage of Carrara marble. *Geophys. Res. Lett.* **38**, 1–6. (doi:10.1029/2011GL049169)

47. Brunauer, S., Emmett, P. H. & Teller, E. 1938 Adsorption of Gases in Multimolecular Layers. *J. Am. Chem. Soc.* **60**, 309–319. (doi:citeulike-article-id:4074706\rdoi: 10.1021/ja01269a023)

48. Yoshioka, N. 1986 Fracture energy and the variation of gouge and surface roughness during frictional sliding of rocks. *J. Phys. Earth* **34**, 335–355.

49. Brantley, S. L. & Mellott, N. P. 1998 Surface Area and Porosity of Primary Silicate Minerals. *Am. Mineral.* **62A**, 229–230. (doi:10.1180/minmag.1998.62A.1.121)

50. Brace, W. F. & Walsh, J. B. 1962 Some direct measurements of the surface energy of quartz and orthoclase. *Am. Mineral.* **47**, 1111–1122.

51. Ben-Zion, Y. & Sammis, C. G. 2013 Shear heating during distributed fracturing and pulverization of rocks. *Geology* **41**, 139–142. (doi:10.1130/G33665.1)

52. Rice, J. R., Sammis, C. G. & Parsons, R. 2005 Off-fault secondary failure induced by a dynamic slip pulse. *Bull. Seismol. Soc. Am.* **95**, 109–134. (doi:10.1785/0120030166)

53. Di Toro, G., Han, R., Hirose, T., De Paola, N., Nielsen, S., Mizoguchi, K., Ferri, F., Cocco, M. & Shimamoto, T. 2011 Fault lubrication during earthquakes. *Nature* **471**, 494–498. (doi:10.1038/nature09838)

CHAPTER 3

GENERAL CONCLUSIONS

3.1 Summary of results

We performed a series of dynamic uniaxial compression tests on Arkansas Novaculite (AN) and Westerly Granite (WG) using a Split-Hopkinson Pressure Bar (SHPB). The critical stress and strain rate thresholds for pulverization in WG – a rock that is representative of some common crustal fault rocks – were comparable to those reported in previous studies using the same rock. The same thresholds for AN – a rock analogous to a homogeneous continuum – however, are significantly higher, yet the yield strength in AN at intermediate strain rates depends strongly on the duration of the applied load.

Distribution of particle sizes in post mortem specimens show a greater portion of large sized fragments resulted from failure of WG samples, compared to failed AN samples. Specific surface area (SSA) measurements obtained via the BET gas adsorption method indicate that a larger portion of the total energy budget of a single dynamic pulverization event under uniaxial compression is dissipated in creating new fracture surfaces for AN specimens than for WG specimens. Moreover, when compared to

slower mechanical grinding, dynamic pulverization of AN produces substantially more new fracture surface area. The opposite is true for WG specimens. Microstructural observations of damaged specimens suggest that tensile, opening mode (mode I) cracking, including some intergranular fracture, is the dominant comminution mechanism in pulverization of AN under dynamic uniaxial compression. Conversely, the microstructures observed in dynamically pulverized WG specimens indicate that minor shearing and possible exploitation of mineral cleavage planes are important mechanisms of grain size reduction in WG.

When corrected for missing submicron particles, specific surface area measurements for dynamically pulverized AN suggest that as much as 40% of dissipated energy in the tests is invested in the creation of new fracture surfaces, whereas only 5% of the energy dissipated in WG tests was invested in new fracture surfaces.

3.2 Contextual discussion

The disparity in both the inelastic yielding response to dynamic compressive loading and the observed post mortem damage between WG and AN intimates that mineral heterogeneity and inherent flaw size exert substantial control on the micromechanical processes active during dynamic pulverization. Specifically, the observed microstructures and relatively high stress and strain rate thresholds of

pulverization in AN indicate that homogeneous continuum models may overestimate the role of mode I fracturing in the pulverization process. Moreover, the apparent utilization of shear on preexisting weak planes in dynamically pulverized WG suggests a complicated partitioning of energy during comminution between distributed frictional heat and new fracture surface, which may depend on the mode of damage (cracking vs. shearing). We speculate that these observations in cm-scale specimens of WG are a microscale analog for activation of small faults and fractures in the damage zones of mature seismogenic faults. Thus, the actual micromechanisms at play during dynamic fracturing and/or pulverization in the process zone of a propagating rupture might depend heavily on the degree of heterogeneity and preexisting damage.

The order of magnitude difference between SSA of our dynamically pulverized specimens and similar measurements on rotary shear produced gouge material suggests that, while dynamic pulverization can act to facilitate comminution in the principal slip zone of a propagating earthquake rupture, subsequent slip wear is probably necessary for generating the extremely fine particle size reduction indicative of natural fault gouge material. This initial grain size reduction may catalyze subsequent rapid weakening mechanisms due to the exposure of fresh particle surfaces, optimizing the activation of physico-chemical weakening processes.

3.3 Future Work

The dynamic load tests in this study were conducted on relatively undamaged rocks, whereas natural fault rocks always have some degree of preexisting damage. Future work should explore the role of preexisting damage by systematically varying initial flaw size and distribution in tested specimens.

All of the dynamic load tests in this study were conducted using a single, half-sine shaped uniaxial compressive pulse. During passage of a dynamic earthquake rupture, the load history experienced within the wall rock may be substantially dissimilar to the loading history during a single SHPB test. Thus, future work will need to focus on replicating more realistic load histories to describe the constitutive inelastic yielding behavior of rocks when subjected to impulsive loads relevant to earthquake ruptures. This is especially true for teasing out the role of tensile loading in dynamically pulverizing fault rocks.